

From Grid to Cloud: Understanding the Impact of Grid Size on Simulated Anvil Clouds and Atmospheric Profiles

Zeyuan Hu¹, Nadir Jeevanjee², and Zhiming Kuang¹

¹Harvard University

²Geophysical Fluid Dynamics Laboratory

October 17, 2023

Abstract

In this study, we explore the relationship between anvil cloud fraction and horizontal model resolution in small domain radiative-convective equilibrium (RCE) simulations, building on the findings of \citeA{jeevanjee22}. Using the System of Atmosphere Modeling (SAM) model, we find that finer resolutions yield higher anvil cloud fractions due to larger convective updrafts mass flux and increased mass detrainment at anvil levels. Employing two different microphysics schemes, we illustrate that finer resolution can enhance mass flux through either stronger cloud evaporation or weaker upper-troposphere stability, as the consequence of enhanced horizontal mixing. Moreover, we refine an analytical zero-buoyancy plume model to investigate the effects of adjusting entrainment rate and evaporation rate on vertical atmosphere profiles in a simple theoretical framework. Our solutions of the zero-buoyancy plume model suggest that stronger horizontal mixing can lead to larger convective updraft mass flux, consistent with the analysis in numerical simulations. We also observe the likelihood of atmospheric profiles converging at a grid size of approximately 100m, potentially as a result of converging entrainment rate and mixing strength. These insights have implications for global storm-resolving simulations, implying a possible convergence of high cloud and deep convection properties as the horizontal resolution approaches around 100m.

1 **From Grid to Cloud: Understanding the Impact of**
2 **Grid Size on Simulated Anvil Clouds and Atmospheric**
3 **Profiles**

4 **Zeyuan Hu¹, Nadir Jeevanjee², Zhiming Kuang^{1,3}**

5 ¹Department of Earth and Planetary Sciences, Harvard University, Cambridge, MA, USA

6 ²Geophysical Fluid Dynamics Laboratory, Princeton, NJ, USA

7 ³John A. Paulson School of Engineering and Applied Sciences, Harvard University, Cambridge, MA, USA

8 **Key Points:**

- 9 • We found a resolution dependence of anvil cloud fraction and updraft mass flux
10 in simulations mostly due to the change of cloud-air mixing.
11 • We derived a self-consistent solution for a zero-buoyancy plume model as a sim-
12 ple tool to understand steady-state tropical atmosphere.
13 • We observed a convergence in atmospheric profiles, including anvil cloud fraction,
14 at a grid resolution of approximately 100m.

Corresponding author: Zeyuan Hu, zeyuan.hu@fas.harvard.edu

Abstract

In this study, we explore the relationship between anvil cloud fraction and horizontal model resolution in small domain radiative-convective equilibrium (RCE) simulations, building on the findings of Jeevanjee and Zhou (2022). Using the System of Atmosphere Modeling (SAM) model, we find that finer resolutions yield higher anvil cloud fractions due to larger convective updrafts mass flux and increased mass detrainment at anvil levels. Employing two different microphysics schemes, we illustrate that finer resolution can enhance mass flux through either stronger cloud evaporation or weaker upper-troposphere stability, as the consequence of enhanced horizontal mixing. Moreover, we refine an analytical zero-buoyancy plume model to investigate the effects of adjusting entrainment rate and evaporation rate on vertical atmosphere profiles in a simple theoretical framework. Our solutions of the zero-buoyancy plume model suggest that stronger horizontal mixing can lead to larger convective updraft mass flux, consistent with the analysis in numerical simulations. We also observe the likelihood of atmospheric profiles converging at a grid size of approximately 100m, potentially as a result of converging entrainment rate and mixing strength. These insights have implications for global storm-resolving simulations, implying a possible convergence of high cloud and deep convection properties as the horizontal resolution approaches around 100m.

Plain Language Summary

High, anvil-shaped clouds in the tropics significantly impact our climate, but simulating them accurately is challenging. Our study reveals that the area these clouds cover in simplified simulations is largely affected by the level of detail in representing the tropical atmosphere. As we refine the simulation resolution, cloud evaporation and the rate of mixing between cloudy and clear air (entrainment) increase, leading to more vigorous updrafts and higher upward mass transport at the level of these high clouds. Consequently, we observe more coverage of high clouds as the simulation resolution improves. Our research indicates that to achieve more realistic cloud simulations, we need to factor in how these processes change with resolution. We expect that the properties of these clouds will begin to converge in the simulations when the grid size reaches approximately the order of 100m.

1 Introduction

Simulating cloud and convection accurately has long been a major challenge for accurate climate and weather simulations. Uncertainty associated with cloud remains as one of the most significant factors contributing to climate feedback uncertainties in future climate change projections (e.g., Bony et al., 2015; Zelinka et al., 2020). In recent years, the scientific community has made significant strides in developing and examining global storm-resolving models (GSRM) with grid sizes of 1-5km (e.g., Satoh et al., 2019; Stevens et al., 2019). By explicitly resolving deep convection, GSRMs can bypass the uncertainties in convective parameterization. A crucial question for using the GSRMs is whether a resolution at the order of 1km is sufficient to resolve relevant atmospheric physical processes.

Resolution dependence in atmosphere models that explicitly resolve deep convection has been extensively studied in various simulation setup. By changing horizontal grid size from 80km to 2.5km in a GSRM, Hohenegger et al. (2020) showed that many 40-day mean, global mean climate statistics, such as precipitation, sensible heat flux, and outgoing longwave radiation, exhibit weak resolution dependence compared with the uncertainties across different GSRMs. However, Hohenegger et al. (2020) also showed some convection and cloud properties, such as the width of the Intertropical Convergence Zone and the fraction of deep convective clouds, have not converged even at 2.5km resolution. Miyamoto et al. (2013) also examined the sensitivity of deep convection to resolution at

65 around the order of 1km in global simulations. They showed that deep convective cores
 66 start to occupy more than one grid point at around 2km and have stronger upward ve-
 67 locity with finer resolution. In idealized squall line simulations, Bryan et al. (2003) showed
 68 decreasing grid size from the order of 1km to the order of 100m tends to give more tur-
 69 bulent flow with resolved entrainment and overturning within clouds. In limited-area 24-
 70 hour simulations with tropical maritime large-scale forcing, Khairoutdinov et al. (2009)
 71 found low sensitivity of quantities such as cloud fraction, relative humidity, and precip-
 72 itation rate to grid size ranging from 100m to 1600m, but updraft core statistics are sen-
 73 sitive to resolution, with finer resolution showing larger upward velocity and more total
 74 water in updraft core. From limited-area radiative-convective equilibrium (RCE) sim-
 75 ulation studies, Jeevanjee (2017) showed that the updraft velocity can keep increasing
 76 with finer resolution until grid size is at the order of 100m. Jeevanjee and Zhou (2022)
 77 found that, in RCE simulation, high cloud fraction exhibits strong resolution dependence,
 78 with finer resolution leading to higher anvil cloud fraction.

79 In the present study, we focus on the resolution dependence of anvil cloud fraction
 80 in RCE simulations. Anvil cloud plays a crucial role in regulating the atmospheric ra-
 81 diation flux, but large uncertainties remain in the modeling of anvil clouds. In a study
 82 from an intermodel comparison project of RCE simulations (Wing et al., 2020), even un-
 83 der very similar setups, different models produce very different anvil cloud fraction and
 84 disagree on the sign of anvil cloud fraction change with warmer sea surface temperature.
 85 Sherwood et al. (2020) reported that cloud feedback uncertainty associated with anvil
 86 clouds is comparable to other types of clouds such as tropical marine low clouds. Anvil
 87 cloud fraction could be thought of as the product of mass detrainment and lifetime of
 88 detrained clouds (e.g., Seeley et al., 2019; Beydoun et al., 2021). The mass detrainment
 89 describes how fast cloud mass is ejected into the atmosphere from deep convective core.
 90 The mass detrainment is closely related to the mass flux of convective updrafts reach-
 91 ing the upper troposphere. The lifetime describes how long the detrained cloud mass can
 92 stay in the atmosphere before removed by evaporation/sublimation and sedimentation.
 93 The lifetime can be sensitive to microphysics parameterization used in the model (e.g.,
 94 Hartmann et al., 2018). Different microphysics schemes can lead to very different anvil
 95 cloud fraction (e.g., see our results in later sections).

96 Jeevanjee and Zhou (2022) (hereafter, JZ22) showed a striking dependence of anvil
 97 cloud fraction on horizontal resolution. In their simulations, they observed that the peak
 98 anvil cloud fraction rises dramatically from approximately 5% at the coarsest 16 km grid
 99 size to over 40% at the finest 62.5 m resolution, with no indication of convergence even
 100 at this highest resolution. They argued that finer horizontal resolution corresponds to
 101 stronger mixing with a shorter mixing timescale, which they defined as the time for a
 102 cloudy grid to completely mixed with a neighboring clear grid. The stronger mixing can
 103 enhance cloud evaporation and lower precipitation efficiency. A smaller precipitation ef-
 104 ficiency would then lead to greater cloud based mass flux, which would lead to more mass
 105 flux reaching upper troposphere and producing more anvil clouds.

106 While the findings in JZ22 offer significant insights, it is intriguing to note the dif-
 107 fering results presented by Bogenschutz et al. (2023). Specifically, they observed that dur-
 108 ing a 20-day simulation with observed large-scale forcing, the anvil cloud fraction is in-
 109 sensitive when the resolution changes from 5km to 500m, whereas in JZ22 the anvil cloud
 110 fraction does not converge even at a grid size of 62.5m. The duration of the simulation
 111 and the presence or absence of large-scale forcing could be influential factors. Notably,
 112 JZ22 ran simulations over a longer period (50 days) to achieve radiative-convective equi-
 113 librium, without including any large-scale forcing. Furthermore, differences in microphysics
 114 and sub-grid turbulence parameterization used in the two studies might also contribute
 115 to the different sensitivity of high clouds.

116 In this study, we would like to further examine the causality in the argument in
 117 JZ22 that enhanced mixing with finer resolution can lead to more convective updraft mass

118 flux in the upper troposphere through increased precipitation efficiency and increased
 119 cloud base mass flux. Jeevanjee (2022) showed that the increase in cloud base mass flux
 120 due to higher precipitation efficiency is not entirely robust, given the unconstrained ef-
 121 fects of entrainment and detrainment. It is also not clear whether changes in cloud base
 122 mass flux can consistently project to the upper troposphere, again considering the un-
 123 constrained effects of entrainment and detrainment.

124 We tested the resolution dependence of anvil cloud fraction in small-domain RCE
 125 simulations with grid size ranging from 4km to 125m. The domain size is fixed across
 126 different simulations. Since the anvil cloud fraction is sensitive to microphysics param-
 127 eterization, we examined the mechanism for the resolution dependence in two different
 128 microphysics schemes. We found that anvil cloud fraction shows sign of convergence when
 129 the grid size is at the order of 100m. Consistent with JZ22, due to enhanced horizon-
 130 tal mixing, finer resolution produces more updraft mass flux in the upper troposphere
 131 and leads to increasing anvil cloud fraction. The stronger mixing in finer resolution leads
 132 to enhanced cloud evaporation and stronger entrainment rate. By examining the clear-
 133 sky energy budgets, we showed that both the enhanced cloud evaporation and the stronger
 134 entrainment rate could contribute to a stronger environmental subsidence and updraft
 135 mass flux.

136 We further used an analytical zero-buoyancy plume model to examine the effects
 137 of changing evaporation rate and entrainment rate in a simple theoretical framework.
 138 We refined the plume model and derived self-consistent solutions of RCE atmosphere pro-
 139 files. We found that increasing entrainment rate can lead to increase of upper troposphere
 140 mass flux through either more cloud evaporation or weaker stability in the upper tro-
 141 posphere. However, increasing evaporation rate alone may not necessarily change the up-
 142 draft mass flux in the upper troposphere. The insights from the analytical plume model
 143 emphasize the role of the horizontal mixing and refine the pathway connecting enhanced
 144 mixing to a stronger upper tropospheric mass flux.

145 The rest of the manuscript is structured as follow: in section 2 we describe the ex-
 146 perimental setup. Section 3 shows our results. Section 3.1 shows the contribution of mass
 147 detrainment and lifetime to the cloud fraction changes. Section 3.2 shows how the stronger
 148 mixing in finer resolution simulations contributes to more updraft mass flux through en-
 149 ergy balance. Section 3.3 shows the results and insights from the analytical solution of
 150 the zero-buoyancy plume model. Section 4 is the discussion and summary.

151 2 Experiment setup

152 We use the System for Atmosphere Modeling (SAM; Khairoutdinov & Randall, 2003),
 153 version 6.10.6, configured as a cloud-resolving model. We run three-dimensional RCE
 154 simulations using the same domain size of 128km \times 128km with different horizontal res-
 155 olution of 4km, 2km, 1km, 500m, 250m, and 125m. All simulations use 60 vertical lev-
 156 els with model top located at 26km and a rigid-lid top boundary condition. The verti-
 157 cal grid spacing increases from 75m near the surface to a constant of 500m through the
 158 whole free troposphere and above. A sponge layer is located in the upper 30% of the model
 159 domain (i.e., above 18km). The radiation scheme is Rapid and Accurate Radiative Trans-
 160 fer Model for General Circulation Models (RRTMG) (Iacono et al., 2008). A simple Smagorinsky-
 161 type scheme (Khairoutdinov & Randall, 2003) is used for the effect of subgrid-scale mo-
 162 tion. We use a constant solar insolation (no diurnal cycle) with fixed solar constant of
 163 683.5 $W m^{-2}$ and zenith angle of 50.5°. Domain-averaged horizontal wind is nudged to
 164 zero at each vertical level with a nudging time scale of 1hour. Sea surface temperature
 165 is fixed uniformly at 303K.

166 We use two different microphysics schemes: SAM single-moment scheme (SAM1MOM,
 167 Khairoutdinov & Randall, 2003) and a double-moment Morrison scheme (Morrison et

168 al., 2005). The SAM one-moment scheme uses an instantaneous saturation adjustment
 169 to generate and remove cloud condensate. Between 0° and -20°C, partitioning of cloud
 170 condensate into cloud ice and liquid water depends linearly on temperature (at -20°C,
 171 all condensate is ice; at 0°C, all condensate is liquid water). More pathways for conver-
 172 sion between different hydrometeors are included in the Morrison double-moment scheme.
 173 The Morrison scheme tends to produce more ice cloud in the upper troposphere (e.g.,
 174 Powell et al., 2012; Hu et al., 2021) and consequently strong atmospheric cloud radi-
 175 ative heating in the middle and upper troposphere. This stronger atmospheric cloud ra-
 176 diative heating can stabilize the upper troposphere and weaken the convective updraft
 177 reaching the upper troposphere (Hu et al., 2021). As we will show later, the weaker up-
 178 per troposphere mass flux will lead to less cloud evaporation in the environment in the
 179 Morrison scheme than in the SAM1MOM scheme.

180 For the simulations with horizontal resolution from 4km to 250m, the first 50 days
 181 are taken as the model spinup and considered long enough for the model to reach equi-
 182 librium. After the 50-day spinup, a 20-day post-equilibrium period is used for analysis.
 183 The 30 samples-per-hour data are then averaged to get an hourly output of domain-mean
 184 statistics. For the 125m-resolution simulation, we initialize the simulation with the equilib-
 185 rium temperature and moisture profile from the 500m-resolution simulation. Then we run
 186 only 30 days for spinup and another 20 days for analysis.

187 3 Results

188 3.1 Cloud fraction change due to mass detrainment

189 Fig. 1 illustrates the resolution-dependent behavior of cloud fraction, atmospheric
 190 cloud radiative effects, and relative humidity. A grid is classified as cloudy if the cloud
 191 mass (the sum of ice and liquid water) mixing ratio exceeds 10^{-5} kg kg⁻¹. As the grid
 192 spacing decreases from 4km to 125m, the peak anvil cloud fraction increases from 7.5%
 193 to 13% in the SAM1MOM simulations (Fig. 1a) and from 17% to 27% in the Morrison
 194 simulations (Fig. 1d). This amplified cloud fraction subsequently leads to increased cloud
 195 radiative heating throughout the majority of the free troposphere (Fig. 1b and 1e). The
 196 cloud fraction profiles appear to converge when the grid spacing falls below 250m in the
 197 SAM1MOM simulations. Along with the increase of the cloud fraction, both the SAM1MOM
 198 and Morrison simulations exhibit a rise in relative humidity throughout the entire free
 199 troposphere with finer resolution (Fig. 1c and 1f).

200 Anvil cloud fraction can be diagnosed as the product of mass detrainment and cloud
 201 lifetime (e.g., Seeley et al. 2019, Beydoun et al. 2022). In Fig. 2, we present profiles of
 202 convective updraft mass flux and in-cloud sedimentation rate to look at the change of
 203 mass detrainment and lifetime change. The convective updraft is characterized by grids
 204 with a vertical velocity greater than 1 m s⁻¹ and a cloud mixing ratio exceeding 10^{-5}
 205 kg kg⁻¹. The in-cloud sedimentation rate is defined as $qcsed/qc$ averaged over cloudy
 206 grids, where qc is the cloud mass (ice plus liquid water) mixing ratio and $qcsed$ is the
 207 tendency of qc due to sedimentation of cloud ice. This sedimentation rate is the major
 208 term of the net removal rate in Beydoun et al. 2022 and could be interpreted as one over
 209 lifetime. Sedimentation rate is positive above around 10 km and negative below, repre-
 210 senting cloud ice falling from detraining level downwards. In both the SAM1MOM and
 211 Morrison simulations, the convective updraft mass flux at above 11km increases with higher
 212 resolution, signifying an increased vertical mass convergence above this altitude. By mass
 213 continuity, the increase of vertical convective mass flux convergence corresponds to an
 214 increase of mass detrainment and an increase of horizontal mass convergence in clear-
 215 sky region. The convective updraft mass flux at middle and lower troposphere shows non-
 216 monotonic change. This is partly due to increased cloud radiative effects with finer res-
 217 olution, which may stabilize the middle troposphere. The sedimentation rate is weaker
 218 for finer resolutions in the SAM1MOM scheme but is slightly stronger in the Morrison

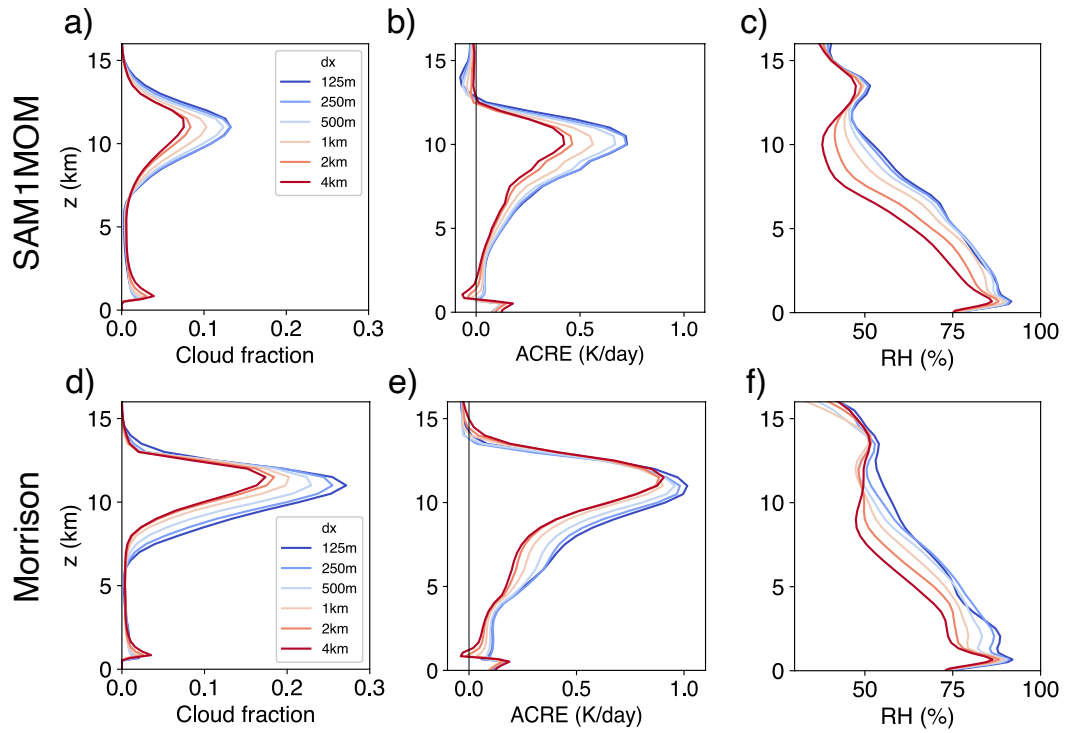


Figure 1. Domain-mean steady-state profiles of cloud fraction (left column), atmosphere cloud radiative effects (middle column) and relative humidity (right column). The upper row corresponds to the SAM1MOM simulations, while the lower row represents the Morrison simulations. Different colors indicate varying grid sizes, with warmer colors denoting coarser resolutions.

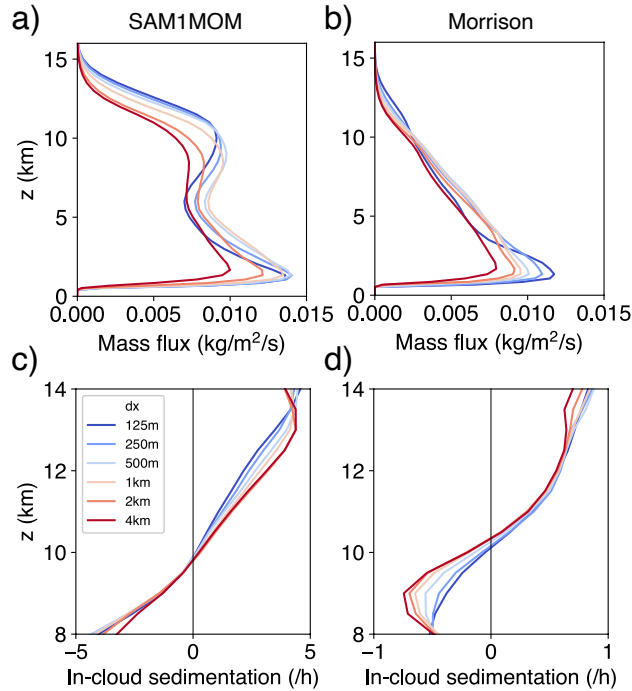


Figure 2. Domain-mean steady-state profiles of convective updraft mass flux (upper row) and cloud ice sedimentation rate (lower row). The left column corresponds to the SAM1MOM simulations, while the right column represents the Morrison simulations. Different colors indicate varying grid sizes, with warmer colors denoting coarser resolutions.

219 scheme. Hence, the observed increase in cloud fraction with finer resolution in both SAM1MOM
220 and Morrison simulations is predominantly driven by the amplification of mass detrainment
221 ment. The contribution from lifetime changes is less certain and could be contingent on
222 the microphysics schemes employed.

223 3.2 Budgets for environmental subsidence

224 In this section, we investigate the mechanisms responsible for the increase in con-
225 vective updraft mass flux associated with finer resolutions. According to the principle
226 of mass continuity, the mass flux in convective updrafts must be balanced by subsidence
227 in the surrounding environment, which we define as grids possessing a cloud mixing ratio
228 less than $10^{-5} \text{ kg kg}^{-1}$. Consequently, elucidating changes in convective updrafts nec-
229 cessitates a corresponding understanding of changes to environmental subsidence. By
230 employing the dry static energy budget of the environment, we decompose the subsidence
231 and will demonstrate that modifications to mass flux profiles could be attributed to changes
232 in both cloud evaporation rate and entrainment rate. The changes in cloud evaporation
233 and in entrainment rate are not purely independent as the change of horizontal mixing
234 can influence both of them. The relative contribution of these two factors will be elab-
235 orated upon in the subsequent section.

236 The dry static energy is defined as $s = c_p T + gz$. The conservation of dry static
237 energy requires

$$238 \frac{\partial s}{\partial t} + \vec{u} \cdot \nabla_h s + w \frac{\partial s}{\partial z} = Q_{rad} + Q_{lat} \quad (1)$$

239 where Q_{rad} is radiative heating, and Q_{lat} is latent heating in the environment. By av-
 240 eraging over all environmental grids and time, and ignoring the time tendency, we obtain:
 241

$$242 \quad \langle \vec{u} \cdot \nabla_h s \rangle + \langle w \frac{\partial s}{\partial z} \rangle = \langle Q_{rad} \rangle + \langle Q_{lat} \rangle \quad (2)$$

243 After further decomposition of $\langle w \frac{\partial s}{\partial z} \rangle = \langle w \rangle \langle \frac{\partial s}{\partial z} \rangle + \langle w' \frac{\partial s'}{\partial z} \rangle$, the averaged environmen-
 244 tal subsidence can be expressed as:

$$245 \quad \langle w \rangle = \frac{\langle Q_{rad} \rangle}{\langle \frac{\partial s}{\partial z} \rangle} + \frac{\langle Q_{lat} \rangle}{\langle \frac{\partial s}{\partial z} \rangle} - \frac{\langle \vec{u} \cdot \nabla_h s \rangle}{\langle \frac{\partial s}{\partial z} \rangle} - \frac{\langle w' \frac{\partial s'}{\partial z} \rangle}{\langle \frac{\partial s}{\partial z} \rangle} \quad (3)$$

246 This equation essentially encapsulates the energy balance within the environment,
 247 implying that the subsidence heating is counterbalanced by the cooling induced by ra-
 248 diation and phase changes in water. In Fig. 3, we show the profiles of latent-driven and
 249 radiation-driven subsidence for the SAM1MOM simulations. The combined effect of latent-
 250 and radiation-driven subsidence closely mirrors the subsidence deduced from model out-
 251 put, and the contribution of advection terms appears minor in comparison to the con-
 252 tribution of radiation and latent heating (not shown).

253 The subsidence near anvil level increases with finer resolution (Fig. 3a), which is
 254 consistent with the change of convective updraft mass flux. In the SAM1MOM simula-
 255 tions, a large portion of the increasing subsidence is counteracted by the negative latent
 256 heating in the environment due to evaporation and sublimation of clouds (Fig. 3b). Con-
 257 versely, negative radiative heating accounts for a relatively smaller portion of this bal-
 258 ance (Fig. 3c). The relative contribution of latent and radiative heating in the Morri-
 259 son scheme is somewhat different. We will probe into the nuances of the Morrison simu-
 260 lations later in this section. It is important to underscore that the role of latent heat-
 261 ing can be influenced by the specific definition of "environment". In our study, the en-
 262 vironment, defined as grids with a cloud mixing ratio less than $10^{-5} \text{ kg kg}^{-1}$, incorpo-
 263 rates grids distanced from clouds as well as those in close proximity to clouds, which ex-
 264 perience evaporation and sublimation from cloud. Results in the following paragraphs
 265 are not sensitive to the choice of cloud threshold. Changing the threshold from $10^{-5} \text{ kg kg}^{-1}$
 266 to $10^{-7} \text{ kg kg}^{-1}$ results in little change. Such insensitivity might be attributed to the model's
 267 procedural steps, wherein evaporation is calculated prior to the output of the cloud mix-
 268 ing ratio. Consequently, grid cells can reflect marginal cloud mixing ratios while still in-
 269 dicating evaporation in the resultant data.

270 The change of latent-driven subsidence is consistent with the change of latent heat-
 271 ing in the environment (Fig. 3d). In the upper troposphere the cooling from phase change
 272 is primarily associated with cloud evaporation/sublimation (Fig. 3e). For simplicity, we
 273 will henceforth use the term "evaporation" to refer to both the evaporation of cloud wa-
 274 ter and sublimation of cloud ice. The cooling due to re-evaporation of precipitation, which
 275 is not displayed here, is less significant than that of clouds in the upper troposphere, al-
 276 though it presents a similar strength in the lower troposphere. We have shown that a
 277 finer resolution model tends to generate more clouds and updraft mass flux. Therefore,
 278 the observed increase in latent cooling might be simply a consequence of the larger amount
 279 of clouds available for evaporation. However, an interesting observation arises when we
 280 normalize the cooling due to cloud evaporation by the domain mean cloud mass mix-
 281 ing ratio (Fig. 3f). Domain mean cloud mixing ratio is proportional to the total cloud
 282 mass in each layer. It becomes evident that, per unit mass, clouds tend to induce a greater
 283 amount of cooling in the environment in the upper troposphere (and also in lower alti-
 284 tudes) when modeled at finer resolution.

285 The observed enhancement in evaporation could be associated with the model res-
 286 olution through the geometric representation of cloud boundaries. We will use clouds at
 287 anvil level as an example, but we assume the intuition behind should apply to clouds at

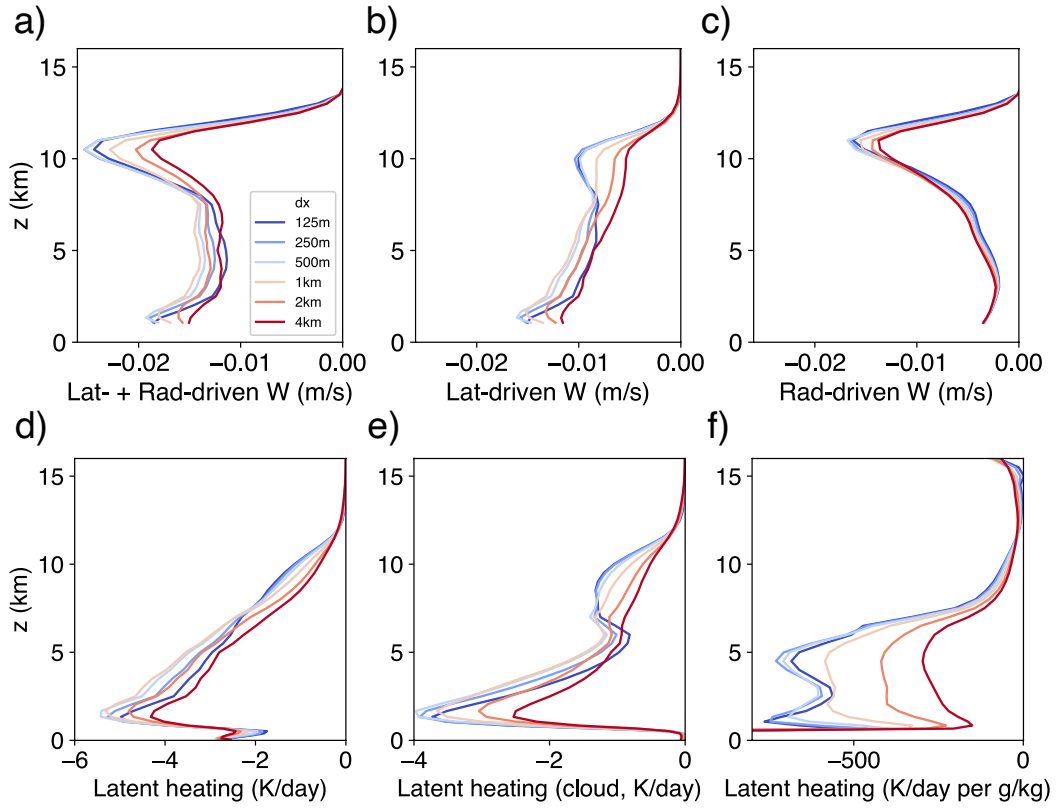


Figure 3. Energy budget for environmental subsidence for the SAM1MOM simulations. The first row shows the subsidence contributed by latent heat (panel b), by radiative cooling (panel c), and by both (a). Panel d shows the latent heating rate averaged in environments. Panel e shows the latent heating rate associated with the phase change between clouds and vapor averaged in environments. Panel f normalizes the cloud-related latent heating rate in panel e by the domain-mean cloud mixing ratio.

288 all the levels. Horizontal snapshots of the cloud mixing ratio at an altitude of $z=10\text{km}$
 289 are depicted in Fig. 4a and 4b. These images represent two $32\text{km}\times 32\text{km}$ subdomains
 290 in the 4km -resolution and 125m -resolution simulations respectively. When compared to
 291 the clouds in the coarser 4km -resolution simulation, the clouds in the 125m -resolution
 292 simulation exhibit more complex boundary structures and tend to be more dispersed.
 293 As a result, clouds modeled at finer resolutions exhibit a higher perimeter area ratio (Fig.
 294 4c). In other words, for a cloud patch of the same area, the total perimeter will be longer
 295 in the simulation with finer resolution. This effect is somewhat analogous to the coast-
 296 line paradox in fractal geometry, where the measured length of a coastline varies depend-
 297 ing on the scale of measurement. The increased perimeter to area ratio exposes a larger
 298 mass of the cloud to the environment, potentially leading to greater evaporation near
 299 the cloud edges.

300 The study by Siebesma and Jonker (2000) explored the fractal nature of cumulus
 301 clouds in Large-Eddy Simulations. They argued that while a coarse grid will underes-
 302 timate cloud surface area, the total sub-grid turbulent transport could become resolu-
 303 tion independent if the grid size is within the inertia subrange. However, in our simu-
 304 lations with a grid size on the order of 1km , sub-grid diffusion in the free troposphere
 305 is minimal. We observed that turning off horizontal sub-grid diffusion of scalars (such
 306 as energy and water) resulted in only minor changes to the profiles of cloud fraction and
 307 environmental evaporation (not shown). The cloud evaporation of deep convection is sub-
 308 stantially influenced by numerical diffusion and can be enhanced by a larger perimeter-
 309 to-area ratio. To illustrate this point, we derived an equation (see Appendix A for com-
 310 plete derivation) that describes the relationship between cloud evaporation in relation
 311 to resolved advection and the perimeter-to-area ratio:

$$312 \quad \frac{Q_{lat,env}}{q_m} = \frac{L}{A} U_{adv} \frac{q_{c,edge} + q_{v,env}^*(1 - RH)}{q_{cld}} \frac{L_v}{2c_p f_{env}} \quad (4)$$

313 The Equation 4 indicates that the evaporation due to horizontal mixing at cloud
 314 edges is dependent on several factors. These include the perimeter-to-area ratio (L/A),
 315 the resolved horizontal velocity near the cloud edge (U_{adv}), the cloud mixing ratio near
 316 the cloud edge ($q_{c,edge}$), the saturation deficit in the environment ($q_{v,env}^*(1 - RH)$), and
 317 the average cloud mixing ratio within cloudy grids (q_{cld}). We verify this equation at the
 318 anvil level, characterized by relatively weak vertical motion near the cloud edge, hence,
 319 making cloud evaporation predominantly attributable to horizontal mixing. Fig. 4d demon-
 320 strates that the diagnosed evaporation using Equation 4 qualitatively aligns with the di-
 321 rect model output. From this equation, it is evident that an increased perimeter to area
 322 ratio can positively contribute to enhanced cloud evaporation. In Appendix A, we delve
 323 into how other terms in Equation 4 vary with model resolution. It is more difficult to
 324 validate Equation 4 at lower levels. In the middle troposphere, clouds are typically very
 325 close to the convective core, and evaporation/condensation associated with vertical mo-
 326 tion may not be neglected. However, we assume the enhanced horizontal mixing and larger
 327 perimeter area ratio should still positively contribute to the enhanced evaporation we
 328 show in Fig. 3f. It is important to note the importance of enhanced horizontal mixing
 329 occurring at all levels, not solely at the anvil level. More efficient evaporation at lower
 330 levels could contribute to mass flux increase at those levels and, by mass continuity, should
 331 have a continuing influence on mass flux at higher levels.

332 In the Morrison simulations, we also observe an enhancement in subsidence near
 333 the anvil level, as shown in Fig. 5a. However, the contribution from latent-driven sub-
 334 sidence (Fig. 5b) is weaker in the Morrison scheme compared to the SAM1MOM scheme.
 335 Primarily, the subsidence change near anvil level is dominated by radiation-driven sub-
 336 sidence (see Fig. 5c). We will discuss more on the reasons for the diminished latent-driven
 337 subsidence near anvil level in the Morrison simulations at the end of this section.

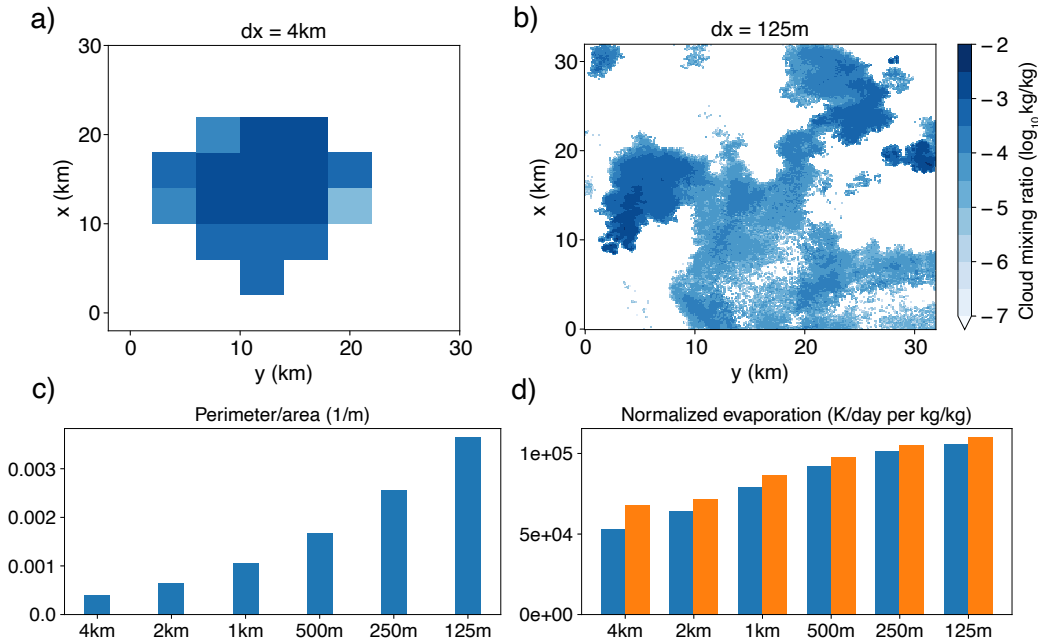


Figure 4. The upper row shows the cloud mixing ratio snapshots at $z=10\text{km}$ in a $32\text{km}\times 32\text{km}$ subdomain in the SAM1MOM simulations with grid size of 4km (a) and 125m (b). Panel c shows the perimeter area ratio in the SAM1MOM simulations with different grid size. Panel d shows the normalized evaporation in Fig. 3f at $z=10\text{km}$. Blue bars are direct model diagnostic values, and orange bars are estimated by Equation 4.

338 We further dissect the radiation-driven subsidence into radiation and stability components.
 339 The radiative cooling shows slight non-monotonic changes (Fig. 5d), while the
 340 upper troposphere is less stable with finer resolution (Fig. 5e and 5f). The change in sta-
 341 bility can be associated with the shift in the entrainment rate (Fig. 6), which tends to
 342 increase with finer resolution. We illustrate this entrainment change with a model of a
 343 spectrum of entraining plumes, following the approach of Kuang and Bretherton (2006).
 344 In this spectrum plume calculations, we use environmental profiles from each simulation
 345 to infer the entrainment rate for updrafts. In Fig. 6a and 6c, we show the convective up-
 346 draft mass flux distribution in the space of frozen moist static energy (FMSE) and height.
 347 FMSE is defined as $c_p T + gz + L_v q - L_f q_i$. The individual lines represent the FMSE
 348 profiles of entraining plumes rising from the cloud base with different entrainment rates.
 349 The convective updrafts in the 125m -resolution simulation (Fig. 6c) shift towards FMSE
 350 profiles with higher entrainment rate compared to the updrafts in the 4km -resolution sim-
 351 ulation (Fig. 6a). Once we have computed the FMSE profiles with varying entrainment
 352 rates, we can measure the amount of mass flux allocated to each entrainment rate bin.
 353 Subsequently, we can represent the updraft mass flux in the space of height and entrain-
 354 ment rate. As shown in Fig. 6b and 6d, it is apparent that the mass flux distribution
 355 shifts towards higher entrainment rates with finer resolution. We have done similar anal-
 356 ysis for the SAM1MOM simulations (not shown) and found consistent results that finer
 357 resolution tends to have higher entrainment rates. However, it is important to note that
 358 the sensitivity of entrainment rate on grid size could be model dependent. In the SAM
 359 model we use, the entrainment mixing seems to be contributed mainly by numerical dif-
 360 fusion, while sub-grid diffusion is very weak in free troposphere. Whether the resolution
 361 dependence of the entrainment rate would hold with other models using different advec-
 362 tion scheme and sub-grid diffusion scheme needs to be further tested.

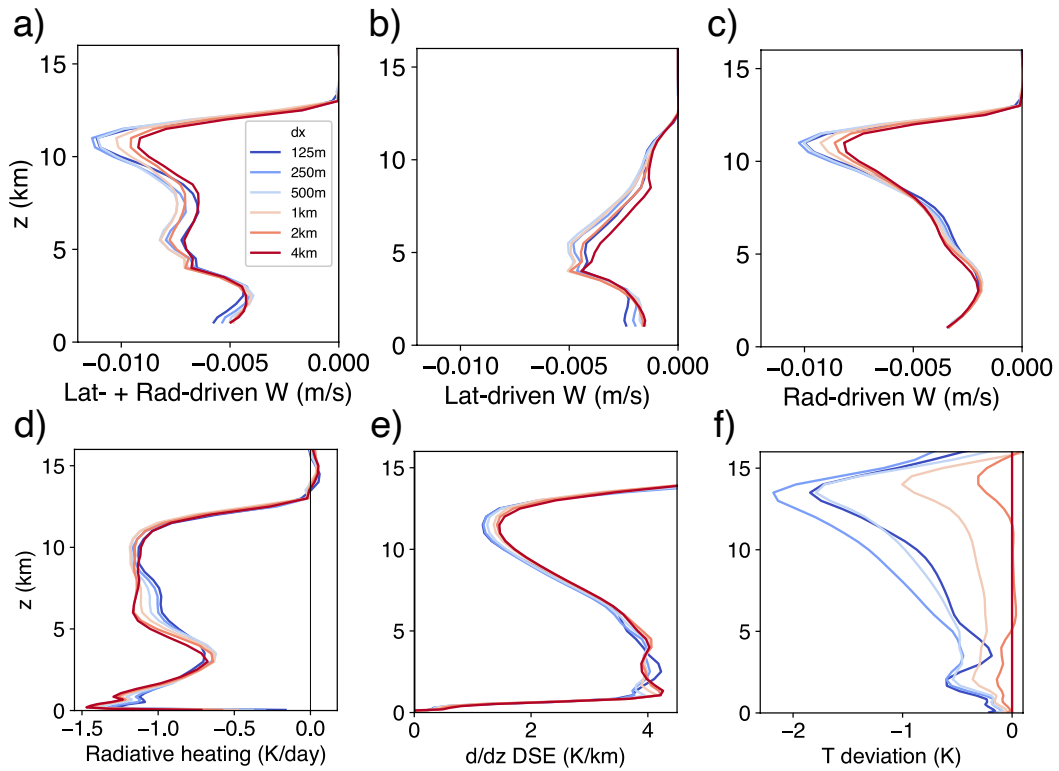


Figure 5. Energy budget for environmental subsidence for the Morrison simulations. The first row shows the subsidence contributed by latent heat (panel b), by radiative cooling (panel c), and by both (a). Panel d shows the radiative heating rate averaged in environments. Panel e shows the vertical gradient of dry static energy averaged in environments. Panel f shows the absolute temperature profiles as deviation to the 4km Morrison simulation.

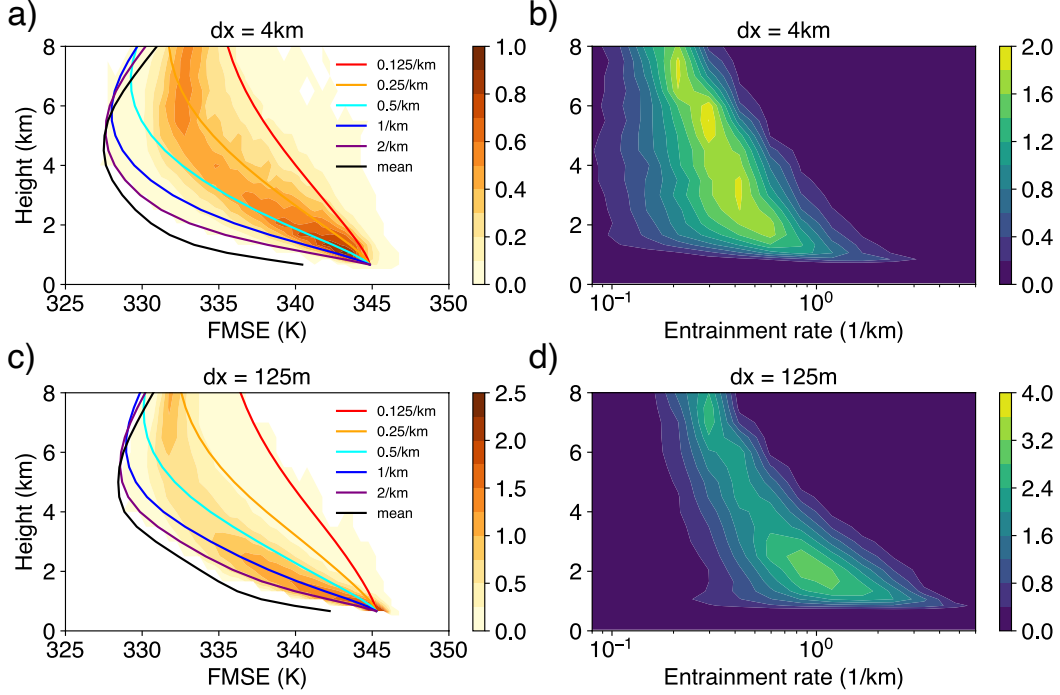


Figure 6. The distribution of convective updraft mass flux in FMSE-height space (left column) and in entrainment-height space (right column) for grid size of 4km (upper row) and of 125m (lower row). In the left column, we show the mass flux distribution (with a unit of a unit of $kg\ m^{-2}\ s^{-1}\ bin^{-1}$) binned by their FMSE (in unit of K). There are 50 bins with 0.5K interval between 325K to 350K. The individual lines represent the FMSE profiles of entraining plumes rising from cloud base with different entrainment rates, except the black line which represents domain-mean FMSE profiles. In the right column, we show the mass flux distribution (with a unit of a unit of $kg\ m^{-2}\ s^{-1}\ bin^{-1}$) binned by their effective entrainment rate. The bin boundaries have entrainment rates of $2^{(i/2)-4}$, for $i = 0, 1, 2, \dots, 16$, with a unit of km^{-1} . We calculated the instantaneous FMSE profiles with these different entrainment rates and sorted the convective updraft mass flux by these different entraining moist-adiabat FMSE values.

Fig. 7 explores the reasons behind the distinctive environmental energy balance regime observed in the Morrison simulations compared to the SAM1MOM simulations. In the Morrison simulations, the cooling effect from evaporation in the upper troposphere is notably weaker than that from radiation. Two factors could account for this subdued evaporation: diminished updrafts and a slower evaporation rate. As previously noted, the Morrison scheme tends to generate more anvil clouds, probably due to the significantly slower ice sedimentation removal rate and prolonged lifetime (refer to Fig. 2). The enhanced cloud radiative heating in the Morrison simulations could stabilize the upper troposphere, thereby reducing the intensity of updrafts. When we disable cloud radiative effects in the Morrison simulations (represented by solid lines in Fig. 7), we observe an increase in upper troposphere convective updrafts and stronger latent-driven subsidence, compared to the default Morrison simulations (dotted lines in Fig. 7). Additionally, the Morrison scheme does not employ saturation adjustment for cloud ice, potentially slowing evaporation compared to the SAM1MOM scheme. When we deactivate the cloud radiative effect and accelerate the cloud ice sublimation rate 100 times to mimic the saturation adjustment (dashed lines in Fig. 7), the result is faster evaporation and intensified updrafts. Consequently, latent-driven subsidence now contributes comparably to radiation-driven subsidence in modifying total subsidence near anvil level as resolution becomes finer (see Fig. 7b to d).

3.3 Insights from an analytical plume model

In the previous section, we presented that stronger horizontal mixing in finer-resolution simulations can enhance cloud evaporation and weaken the stability through a stronger entrainment rate. Both factors could potentially contribute to an enhanced convective updraft mass flux through the energy balance of environmental subsidence. However, a budget analysis does not necessarily reveal causality. Thus, in this section, we employ an analytical plume model to qualitatively explore the separate causal effects of changes in cloud evaporation and entrainment. This dissection of entrainment and evaporation effects offers us the opportunity to refine our understanding of the mechanism that bridges horizontal mixing with convective updraft mass flux.

The analytical plume model we use here is adapted from the zero-buoyancy plume model in Singh and Neogi (2022), with further references to Romps (2014), Singh et al. (2019), and Romps (2021). Here we provide a brief description of the model setup with the full description in Appendix B. The model presented in Singh and Neogi (2022) includes a thermodynamic component and a dynamic component. The thermodynamic component solves the equilibrium state of a moist atmosphere, and the dynamic component couples the thermodynamic component to large-scale circulation. In this study, we utilize only the thermodynamic model to examine radiative-convective equilibrium with no large-scale vertical velocity. It's crucial to distinguish between the analytical plume model used in this section and the spectrum plume model used for calculating the entrainment rate in the previous section. The latter utilizes the environmental profile from each simulation to determine a spectrum of entrainment rates for updrafts. Conversely, the analytical plume model in this section solves for the environmental profiles based on given surface boundary conditions and specified mixing strength and evaporation rate.

The thermodynamic model assumes that the steady state of the atmosphere can be represented by updrafts in a single updraft plume and downdrafts in environment. The updraft and environment can exchange mass, water, and heat via entrainment and detrainment. The model assumes that the steady state of the atmosphere is neutrally buoyant with respect to the entraining plume (Singh & O’Gorman, 2013). The model further presumes that the radiative cooling rate is a function of temperature, i.e., $-1K\ day^{-1}$ when the temperature is above 250K, and gradually decays to 0 at 200K. By solving conservation equations of mass, water vapor, and moist static energy, this model can solve the vertical atmosphere profiles given surface boundary conditions.

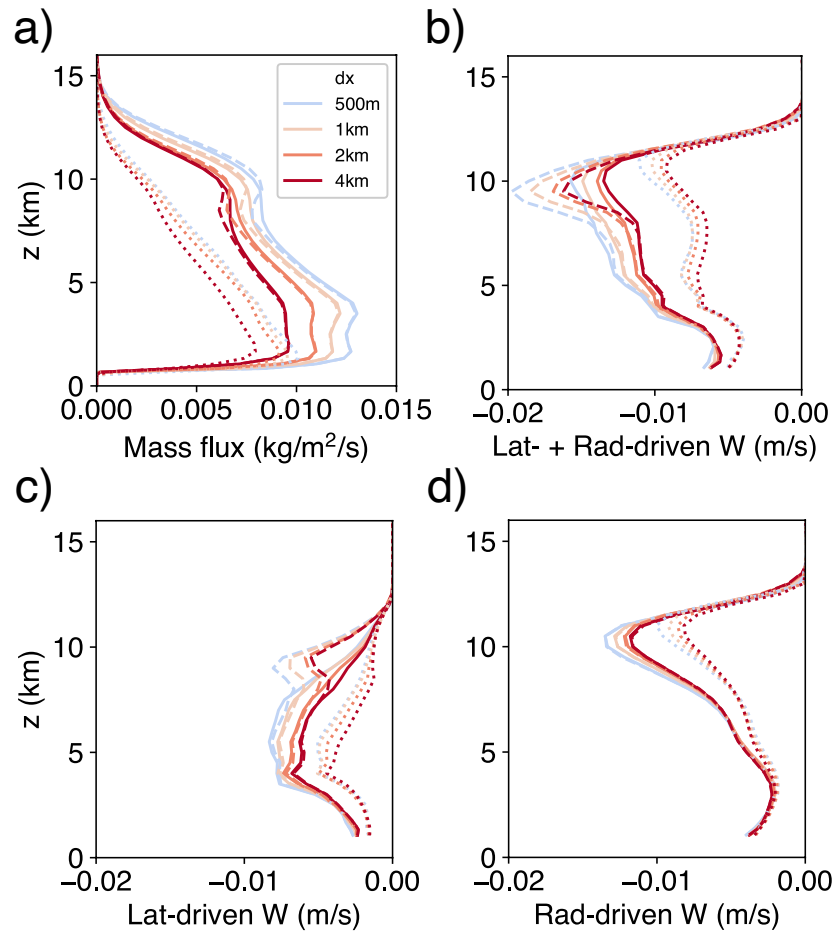


Figure 7. Convective updraft mass flux and energy budget for environmental subsidence in modified Morrison simulations. Solid lines represent simulations where cloud radiative effects are deactivated. Dashed lines indicate simulations with both cloud radiative effects deactivated and expedited cloud ice sublimation. Dotted lines represent default Morrison simulations. Panel a displays the convective updraft mass flux. Panels b to d present the subsidence contributions from latent heat (panel c), radiative cooling (panel d), and a combination of both (panel b).

One caveat of the solutions provided in Singh and Neogi (2022) and Romps (2021) is the assumption of equal fractional entrainment rate and detrainment rate, which in principle should suggest no vertical change in the convective updraft mass flux through the mass conservation equation:

$$\frac{\partial M_c}{\partial z} = M_c(\epsilon - \delta) \quad (5)$$

where M_c is updraft mass flux, ϵ is fractional entrainment rate, and δ is fractional detrainment rate. However, their solution of mass flux profile, e.g., Fig. 7 in Singh and Neogi (2022), does not follow this assumption, especially in the upper troposphere where mass flux rapidly decreases. In this study, we developed a self-consistent method of solving the equations by allowing the difference between fractional detrainment rate and fractional entrainment rate to vary vertically and not imposing any vertically structure on mass flux profile. The shape of the mass flux profile is partially constrained by energetics, as the mass flux needs to diminish where radiative cooling starts to rapidly decrease in the upper troposphere. Therefore, the entrainment rate and detrainment rate cannot be completely independent. Yet, one must still specify the strength of turbulent mixing in the model. This could be represented by either the entrainment rate, detrainment rate, or some other variable, such as the mixing rate in Bretherton et al. (2004). Here we choose to specify the entrainment rate to impose the strength of turbulent mixing. Once we specify the fractional entrainment rate profile (ϵ) and an evaporation parameter (μ), we can determine the vertical atmosphere profiles given boundary conditions (temperature, pressure, and relative humidity at cloud base).

In this model, cloud evaporation is parameterized as:

$$s_{evap} = \mu d(q^* - q) \quad (6)$$

where d is mass detrainment, q^* and q is the specific humidity in saturated updraft and in environment. A larger evaporation parameter μ tends to produce more cloud evaporation in the environment. This equation has two underlying assumptions. First, this equation assumes that the detrained flux of condensate is proportional to detrained flux of water vapor, represented by dq^* . A component of μ quantifies this relationship, representing the amount of condensate present in the detrained air. Second, it assumes that the fraction of detrained condensate that evaporates - as opposed to precipitating to the ground - is proportional to $1 - q/q^*$, which equates to $1 - RH$. A component of μ quantifies this relationship, reflecting the relative rates of evaporation versus conversion to rain. It is likely that the ratio of condensate evaporation versus conversion to rain is less sensitive to RH when RH is far less than 1. We also explored a different parameterization defined by $s_{evap} = \mu dq^*(1 - RH)^{0.5}$, which yielded results that are qualitatively similar (not shown). The full details of the model equations, derivation of the solution, and some sensitivity tests are documented in Appendix B.

With this model, we now test the sensitivity of the steady-state atmosphere profiles to entrainment rate and evaporation rate. First, we test the sensitivity to the fractional entrainment rate ϵ for two different values of the evaporation parameter μ (Fig. 8, upper row for $\mu = 1$ and lower row for $\mu = 0.1$). In both cases, with an increase in entrainment rate, we observe an increase in detrainment rate, mass flux, relative humidity, and the amount of latent cooling in the environment. The temperature in the upper troposphere is colder with a higher entrainment rate, and the stability (ds/dz) is lower. Fig. 8 suggests that increasing entrainment rate can lead to a relatively uniform increase of mass flux from cloud base to anvil level, although the budget for environmental subsidence can look like different regimes.

Considering the dry static energy budget $M_c = (Q_{rad} + Q_{lat})/(\frac{\partial s}{\partial z})$, increasing entrainment rate leads to both increasing cloud evaporation and more unstable upper troposphere. Both these two factors can contribute to an increasing mass flux. When cloud evaporation is efficient (Fig. 8 with $\mu = 1$), the change of latent cooling can dominate the change of mass flux. However, when cloud evaporation is weak (Fig. 8 with $\mu =$

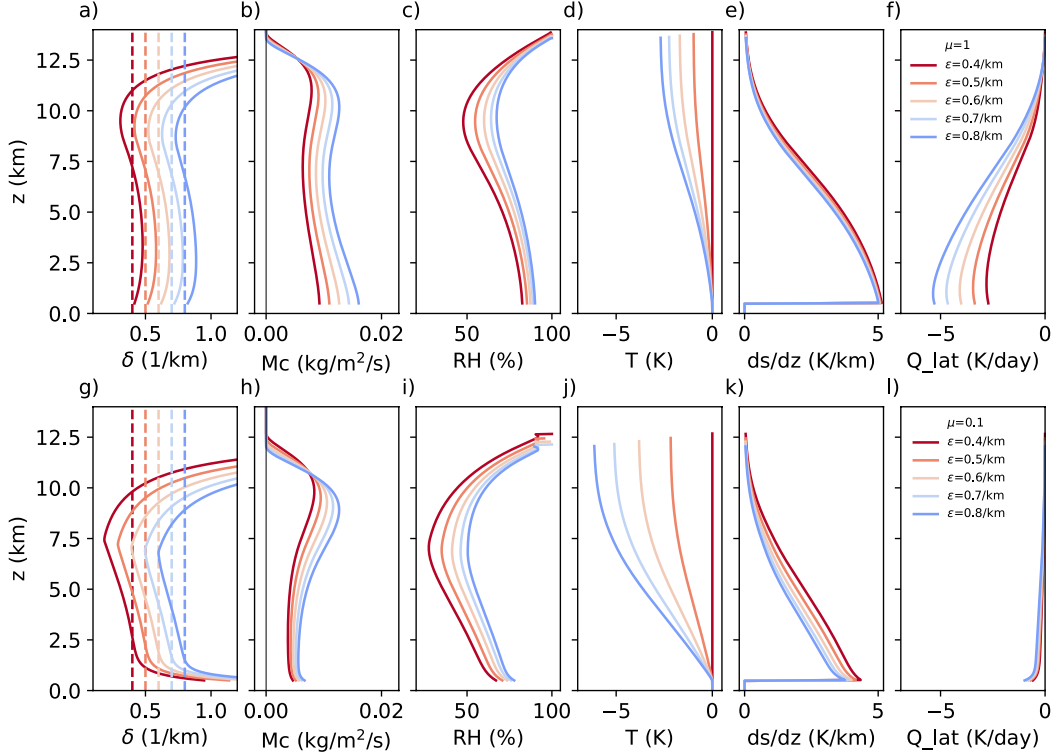


Figure 8. Atmosphere profiles in the zero-buoyancy plume model with varying entrainment rates (warmer color represents lower entrainment rate). The upper row has a cloud evaporation parameter $\mu=1$. The variables shown are detrainment rate (a), updraft mass flux (b), relative humidity (c), temperature (d), vertical gradient of dry static energy (e), and latent heating rate due to cloud evaporation in the environment (f). Dashed lines in panel a are the profiles of prescribed entrainment rate. The temperature in panel d is shown as deviation to one of the simulations, which is denoted by the red line with zero deviation. The lower row is similar to the upper row but with cloud evaporation parameter $\mu=0.1$.

467 0.1), the absolute latent cooling and the change of latent cooling is small compared to
 468 the prescribed radiative cooling. The change of stability to increasing entrainment rate
 469 is larger with small μ and can dominate the change of mass flux. Environmental rela-
 470 tive humidity is important in determining the sensitivity of stability to changing entrain-
 471 ment rate. The relative humidity is smaller with $\mu=0.1$ than $\mu=1$ (Fig. 8c and i). Since
 472 entrainment affects stability through the environmental saturation deficit, a small μ tends
 473 to make stability more sensitive to the change of entrainment (Fig. 8e and k).

474 The energy balance regime with small evaporation parameter resembles that in the
 475 Morrison simulations in the previous section. The Morrison scheme likely has a smaller
 476 evaporation parameter for cloud ice evaporation than the SAM1MOM scheme, due to
 477 the avoidance of saturation adjustment in Morrison scheme, potentially contributing to
 478 the weak absolute latent cooling rate. However, the stability change is not that large be-
 479 tween Morrison and SAM1MOM scheme, comparing to the difference between the ana-
 480 lytical plume results with $\mu=0.1$ and $\mu=1$. The Morrison simulations also have slightly
 481 higher relative humidity in the upper troposphere compared to the SAM1MOM simu-
 482 lations. The main difference between the Morrison and the SAM1MOM simulations is
 483 the diminished environmental latent cooling instead of the stability change.

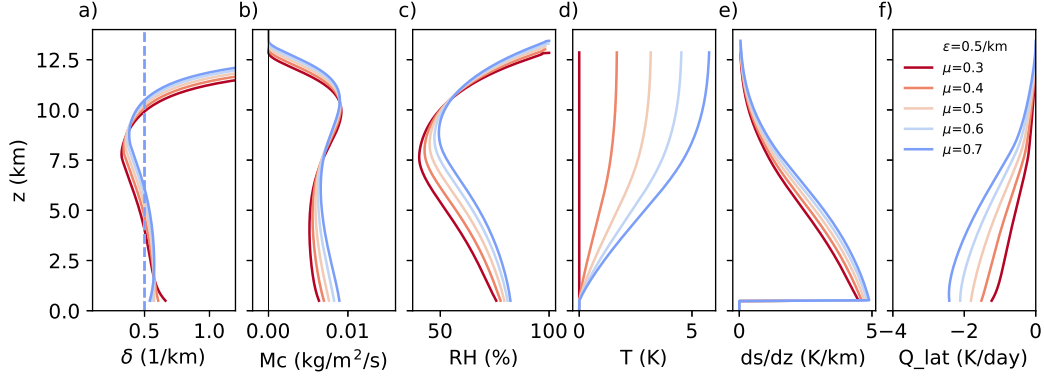


Figure 9. Similar to Fig. 8 but with fixed entrainment rate of 0.5 km^{-1} and varying cloud evaporation parameter (warmer color represents less efficient cloud evaporation).

484 In Fig. 9, we maintain a constant fractional entrainment rate as 0.5 km^{-1} and test
 485 the sensitivity of atmosphere profiles to the evaporation parameter μ . As the evapora-
 486 tion strength increases, we can see that the free troposphere is warmer, deeper, and more
 487 moist (Fig. 9b,9c,9d). The increased relative humidity is a direct result of the enhanced
 488 efficiency of cloud evaporation. This is consistent with JZ22 which shows that the evap-
 489 oration efficiency plays an important role for the relative humidity, especially in the up-
 490 per troposphere. Consequently, with a more moist atmosphere, the dilution of the up-
 491 draft plume due to entrainment is mitigated, resulting in a warmer and elevated tropo-
 492 sphere. In lower troposphere, we see a clear increase of mass flux with increasing cloud
 493 evaporation. However, in the upper troposphere, the mass flux adjustment is more akin
 494 to a upward shift with weak change in magnitude. The peak mass flux near the anvil
 495 level remains largely unchanged, suggesting a minor change in the convergence of mass
 496 flux at higher altitudes. From the perspective of the energy budget, an increase in the
 497 evaporation rate could induce greater latent cooling. However, this is offset by an increase
 498 in stability in the upper troposphere, effectively suppressing the change in mass flux (Fig.
 499 9e and 9f).

500 From Fig. 8 and Fig. 9, we can see that the resolution dependence of updraft mass
 501 flux may not necessarily be driven by evaporation efficiency alone. However, updraft mass
 502 flux can simply be interpreted as a response to the change of entrainment rate or the strength
 503 of horizontal mixing. In addition to the energy budget, a different way to understand
 504 the mass flux response to entrainment rate change in this analytical model is through
 505 the Betts’s rule described in Jeevanjee (2022). Considering the water vapor budget for
 506 the atmosphere above a certain level z . The mass flux at z satisfies:

$$507 \quad M_c q^* (1 - RH) = \int_z^{top} -c_p \rho Q_{rad} dz / L_v \quad (7)$$

508 where q^* is the saturation vapor mixing ratio, c_p is the isobaric specific heat, ρ is air den-
 509 sity, L_v is the latent heat of vaporization. The left hand side (LHS) represents the net
 510 water vapor transported upward across level z by saturated updraft and unsaturated sub-
 511 sidence. In steady state, this transport of vapor must be balanced by the net conden-
 512 sation, which is required to balance the total radiative cooling above level z (the right
 513 hand side, RHS). Since in the model the prescribed the radiative cooling is constant at
 514 -1 K day^{-1} for troposphere where temperature is larger than 250K, the change in RHS
 515 is relatively small, especially for the lower and middle troposphere. When we increase
 516 the horizontal mixing (Fig. 8), the relative humidity increases, and more clouds get de-
 517 trained. The temperature through the whole troposphere also decreases, leading to a de-

518 creasing saturation vapor mixing ratio q^* . To satisfy the equation, the mass flux on the
 519 LHS has to increase to provide enough upward vapor transport.

520 4 Conclusions and Discussion

521 In this work, we investigated the mechanisms underlying the dependence of anvil
 522 cloud fraction on horizontal model resolution in small domain radiative-convective equi-
 523 librium (RCE) simulations. Our findings indicate that finer resolutions yield a larger anvil
 524 cloud fraction due to increased convective updrafts mass flux and enhanced mass detrain-
 525 ment at anvil levels, aligning with Jeevanjee and Zhou (2022) (hereafter JZ22). Further
 526 examination revealed contributing processes to the mass flux increase near the anvil level.
 527 We leveraged two distinct microphysics schemes—one a single-moment scheme, the other
 528 a double-moment Morrison scheme—to reveal that finer resolutions enhance cloud evap-
 529 oration efficiency and entrainment rate, both of which are the consequence of enhanced
 530 horizontal mixing and could contribute to changes in mass flux.

531 In addition, we used an analytical zero-buoyancy plume model (Romps, 2014; Singh
 532 et al., 2019; Romps, 2021; Singh & Neogi, 2022) to further examine the mechanisms link-
 533 ing horizontal mixing to the change of mass flux. We refined the analytical plume model
 534 to derive self-consistent solutions of steady-state atmosphere profiles. This analytical model
 535 can serve as a simple, nice framework to understand general behaviors of RCE. Here, this
 536 model was employed to independently test the effects of modifying fractional entrain-
 537 ment rate and evaporation rate on mass flux and other atmospheric variables. Our anal-
 538 ysis revealed that increasing the fractional entrainment rate bolsters mass flux at both
 539 cloud base and near anvil level, whereas solely augmenting the evaporation rate primar-
 540 ily intensifies the mass flux in the lower troposphere with minimal impact on mass flux
 541 in the upper troposphere. By increasing the fractional entrainment rate alone, we ob-
 542 served that the increase of updraft mass flux can be attributed to either stronger latent
 543 cooling due to cloud evaporation or weaker upper-troposphere stability. The relative im-
 544 portance of these two processes may depend on evaporation rate. When the specified evap-
 545 oration rate is lower, environmental relative humidity is lower, and the lapse rate is more
 546 sensitive to the change of entrainment rate.

547 The results from analytical solution confirms that changes in the horizontal mix-
 548 ing can drive the resolution dependency of mass flux and cloud fraction found in the nu-
 549 merical simulations. One insight from our study, in comparison to JZ22, is that in cer-
 550 tain numerical simulations and analytical scenarios, the change in upper-tropospheric
 551 mass flux is predominantly driven by changes in stability resulting from modifications
 552 in the entrainment rate. Conversely, JZ22 attributes the increase of upper-tropospheric
 553 mass flux with finer resolution solely to the change in precipitation efficiency.

554 We observed that atmospheric profiles like cloud fraction and relative humidity start
 555 to converge when the grid size approximates 100m. The convergence when the grid size
 556 is at the order 100m may be linked to the convergence of entrainment rate and the mix-
 557 ing strength. We do not have a clear theory for the dependence of entrainment rate on
 558 horizontal resolution yet. A potential explanation is that coarser resolution inadequately
 559 resolves turbulent flow and cloud entrainment, and changes in sub-grid diffusion are in-
 560 sufficient to offset the changes in resolved turbulence. Bryan et al. (2003) demonstrated
 561 that a Smagorinsky-like sub-grid scheme is ill-suited for a grid size on the order of 1km.
 562 An inertial subrange can only manifest when the grid size is on the order of 100m. There-
 563 fore, it is plausible that once the grid size is sufficiently refined, changes in sub-grid dif-
 564 fusion can effectively counterbalance changes in numerical diffusion, leading to a con-
 565 vergence in entrainment rate and mixing strength. An ideal sub-grid turbulence param-
 566 eterization should make the entrainment strength scale insensitive even with resolution
 567 at the order of 1km. This might be one reason why Bogenschutz et al. (2023) found less
 568 sensitivity of high cloud fraction compared to this study and to JZ22.

569 The mechanisms we proposed is based on the radiative-convective equilibrium con-
 570 dition. Consequently, the resolution dependence of atmospheric profiles we observed may
 571 not persist when large-scale forcing overwhelms local convective adjustment or when a
 572 simulation has not reached an equilibrium state. This likely accounts for why Khairoutdinov
 573 et al. (2009) did not find the resolution dependence of cloud fraction with finer grid size
 574 in their 24-hour simulations with observed large-scale thermodynamic forcing.

575 Our study has implications to global storm-resolving simulations. Based on the con-
 576 vergence behavior in our small-domain simulations, the properties of cloud and convec-
 577 tion in global storm-resolving simulations may start to converge when the horizontal res-
 578 olution reaches the order of 100m. The exact resolution sensitivity can be model depen-
 579 dence. Also, it is not clear whether the same resolution dependence we learned in small-
 580 domain simulation—increasing resolution leading to more convective updrafts and cloud
 581 fraction—can be directly applied to the tropics in global storm-resolving simulations. The
 582 influence of horizontal resolution on cloud fraction or mass flux profiles could vary or even
 583 reverse if changing grid size changes the degree of large-scale aggregation of deep con-
 584 vection (e.g., Becker et al., 2017). Future research could focus on investigating these po-
 585 tential differences to better understand the uncertainties and biases inherent in global
 586 storm-resolving simulations.

587 5 Open Research

588 The atmosphere model used to run the simulations is the System for Atmospheric
 589 Modeling (Khairoutdinov & Randall, 2003) and is available at [http://rossby.msrc.sunysb](http://rossby.msrc.sunysb.edu/~marat/SAM.html)
 590 [.edu/~marat/SAM.html](http://rossby.msrc.sunysb.edu/~marat/SAM.html) (version 6.10.6, Khairoutdinov, 2023). The figures in this manuscripts,
 591 created by Python version 3.9, can be reproduced using the codes and data stored at [https://](https://doi.org/10.5281/zenodo.8397768)
 592 doi.org/10.5281/zenodo.8397768 (Hu et al., 2023).

593 Appendix A Relationship between cloud evaporation and perimeter 594 area ratio

595 In the preceding sections, we highlighted the increased perimeter area ratio of cloud
 596 mass at higher resolutions, which potentially leads to a greater exposure of the cloud mass
 597 to an unsaturated environment, thereby amplifying cloud evaporation. In this section,
 598 we derive a quantitative relationship between the cloud evaporation rate and the prime-
 599 ter area ratio.

600 Consider a specific level with a unit thickness, where the cloud mass has a total
 601 area (A) and total perimeter (L). The clouds are advected in grid points through resolved
 602 horizontal wind with a representative speed of U_{adv} . Approximately half of the cloud bound-
 603 ary exhibits horizontal resolved wind pointing outwards from the cloud, while the other
 604 half features wind directed inward (Fig. A1). After a time step dt , the volume of clouds
 605 advected across the boundary amounts to $0.5LU_{adv}dt$ (represented by the yellow area
 606 in Fig. A1a). An equivalent volume of environmental air is advected into the original
 607 cloudy grids (illustrated by the orange area in Fig. A1a). Following advection, the SAM1MOM
 608 scheme performs saturation adjustment. The yellow cloud mass becomes fully mixed with
 609 the environmental air in the respective grids, subsequently evaporating. On average, since
 610 the cloud mixing ratio near cloud edges is relatively minimal, we assume complete evap-
 611 oration of the yellow cloud mass. The evaporation associated with this yellow cloud mass
 612 should be proportional to the product of the volume and the cloud mixing ratio at the
 613 edge $q_{c,edge}$. Similarly, in the grids containing orange environmental air, a portion of the
 614 cloud must evaporate to bring the unsaturated orange environmental air to saturation.
 615 The evaporation amount would be the product of the volume and the saturation deficit
 616 $q_{v,env}^*(1 - RH)$, where $q_{v,env}^*$ represents the environmental saturation specific humid-
 617 ity and RH denotes relative humidity. The total evaporation rate associated with sat-

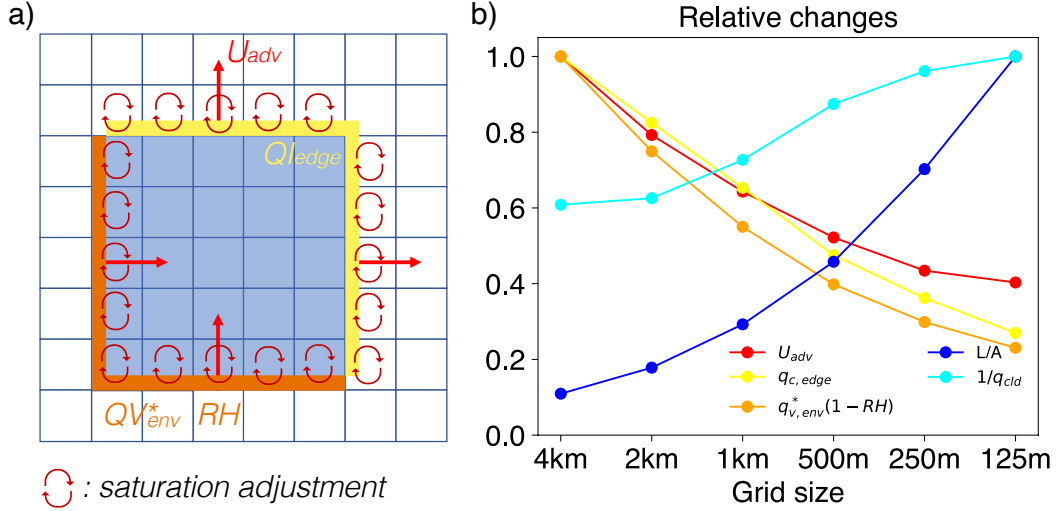


Figure A1. Panel a shows a schematic of cloud evaporation due to resolved horizontal advection and the following saturation adjustment in the SAM1MOM scheme. We set some cloud initially in the grids with blue shading and advect the cloud by horizontal wind with $U_x = U_y = U_{adv}$. $q_{c,edge}$ is the cloud mixing ratio near the cloud edge. $q_{v,env}^*$ represents the environmental saturation specific humidity, and RH denotes relative humidity in the environment near the cloud. After a small timestep dt , some cloud mass is advected into environment grids (yellow shading), and some environmental mass is advected into cloudy grids (orange shading). Circular arrows represent the saturation adjustment in each grid due to microphysics scheme. Panel b shows the relative value of different terms in Equation A4 in the SAM1MOM simulations with different resolution. Each term is standardized (divided by the maximum value across the simulations with different resolution) to have a value between 0 and 1.

618 uration adjustment can be expressed as:

$$619 \quad \text{Evaporation} = 0.5LU_{adv}\rho[q_{c,edge} + q_{v,env}^*(1 - RH)] \quad (\text{A1})$$

620 We assume all this evaporation can be counted as in the environment. We further as-
 621 sume the total evaporation in the environment is dominated by this numerical diffusion
 622 associated with resolved horizontal wind. This assumption likely works well for high clouds
 623 where vertical wind and sub-grid diffusion are weak, but may not work well for low clouds
 624 where vertical wind and sub-grid diffusion could be strong. Total air mass in the envi-
 625 ronment can be written as $\rho A_d f_{env}$, where A_d is domain area, f_{env} is the fraction of en-
 626 vironment. Therefore, the latent heating rate in the environment can be written as:

$$627 \quad Q_{lat,env} = 0.5LU_{adv}[q_{c,edge} + q_{v,env}^*(1 - RH)] \frac{L_v}{c_p A_d f_{env}} \quad (\text{A2})$$

628 Since more clouds tend to generate more evaporation, we normalize the latent heating
 629 by the total cloud mass to get a quantity that reflect evaporation efficiency. Total cloud
 630 mass is proportional to the domain-mean cloud mixing ratio q_m , which can be further
 631 expressed as $q_m = f_{cld} q_{cld}$. f_{cld} is cloud fraction, and q_{cld} is the cloud mixing ratio av-
 632 eraged in cloudy grids. The normalized latent heating rate can be expressed as:

$$633 \quad \frac{Q_{lat,env}}{q_m} = 0.5LU_{adv}[q_{c,edge} + q_{v,env}^*(1 - RH)] \frac{L_v}{c_p A_d f_{env} f_{cld} q_{cld}} \quad (\text{A3})$$

634 Note that total cloud area can be written as $A = f_{cld} A_d$, the above equation can be
 635 rewritten as:

$$636 \quad \frac{Q_{lat,env}}{q_m} = \frac{L}{A} U_{adv} \frac{q_{c,edge} + q_{v,env}^*(1 - RH)}{q_{cld}} \frac{L_v}{2c_p f_{env}} \quad (\text{A4})$$

637 We define cloud boundaries as grid interfaces that separate a grid with zero cloud
 638 mixing ratio from a grid with non-zero cloud mixing ratio. Subsequently, we evaluate
 639 the average values of U_{adv} , $q_{c,edge}$, $q_{v,env}^*$, and RH at grids immediately adjacent to the
 640 boundaries, either on the inside or the outside. In Fig. A1b, we demonstrate the vari-
 641 ation in different terms of Equation A4 as resolution becomes finer. With increased res-
 642 olution, the perimeter area ratio rises, while advection velocity, cloud mixing ratio, and
 643 environmental saturation deficit decrease. The decline in near-edge cloud mixing ratio
 644 and environmental saturation deficit could be attributed to the improved representation
 645 of the transition between cloudy grids and environmental grids at finer scales. The en-
 646 hanced transition at cloud boundaries in higher resolutions tends to reduce numerical
 647 diffusion and partially counterbalance the effect of the growing perimeter area ratio. The
 648 cause of the weakened advection wind and reduced in-cloud mixing ratio remains unclear
 649 and merits further investigation.

650 Overall, finer resolution enables better representation of turbulent cloud bound-
 651 aries, which can enhance the interaction between clouds and their environment. How-
 652 ever, finer resolution also leads to a reduction in numerical diffusion. The interplay be-
 653 tween these two effects may be crucial in determining whether cloud evaporation effi-
 654 ciency converges at a specific resolution. A comprehensive understanding of these fac-
 655 tors is essential for improving the accuracy and reliability of Earth system models.

656 **Appendix B Refined solutions of a zero-buoyancy plume model**

657 Here we document the details of how we solve the zero-buoyancy plume model to
 658 get self-consistent solutions about steady-state mass flux, detrainment rate, and other

659 atmosphere profiles. The equations we solve are:

$$660 \quad \frac{\partial M_c}{\partial z} = e - d \quad (\text{B1})$$

$$661 \quad M_c + M_e = 0 \quad (\text{B2})$$

$$662 \quad \frac{\partial(M_c q^*)}{\partial z} = e q - d q^* - s_{cond} \quad (\text{B3})$$

$$663 \quad \frac{\partial(M_e q)}{\partial z} = d q^* - e q + s_{evap} \quad (\text{B4})$$

$$664 \quad \frac{\partial(M_c h^*)}{\partial z} = e h - d h^* \quad (\text{B5})$$

$$665 \quad \frac{\partial(M_e h)}{\partial z} = d h^* - e h + Q_{rad} \quad (\text{B6})$$

$$666 \quad h^* - h = L_v (q^* - q) \quad (\text{B7})$$

$$667 \quad s_{evap} = \mu d (q^* - q) \quad (\text{B8})$$

$$668 \quad \frac{\partial p}{\partial z} = -\frac{\rho g}{R_d T} \quad (\text{B9})$$

670 Equation B1 and B2 are mass conservation equations. M_c is the mass flux of con-
 671 vective updrafts, and M_e is mass flux in the environment. We assume there is no large-
 672 scale advection, so the net mass flux in updrafts and in environment is 0. e is mass en-
 673 trainment, and d is mass detrainment. Fractional entrainment rate ϵ and fractional de-
 674 trainment rate δ are defined as:

$$675 \quad \epsilon = e/M_c \quad (\text{B10})$$

$$676 \quad \delta = d/M_c \quad (\text{B11})$$

678 Equation B3 and B4 describes the water vapor conservation in updraft plume and
 679 in environment separately. q is the water vapor mixing ratio in the environment. q^* is
 680 the saturation vapor mixing ratio in the updraft plume, which is simply a function of
 681 temperature and pressure:

$$682 \quad q^* = 0.622 p_v^*/p = 0.622 \frac{p_0}{p} e^{-\frac{L_v}{R_v T}} \quad (\text{B12})$$

684 where $p_v^* = p_0 \exp(-L_v/(R_v T))$ is the saturation vapor pressure, $L_v=2.51e6 \text{ J kg}^{-1}$
 685 is the latent heat of condensation, $R_v= 461 \text{ J kg}^{-1} \text{ K}^{-1}$ is gas constant for water vapor,
 686 $p_0=2.69e11 \text{ Pa}$ is a constant.

687 Equation B5 and B6 describes the conservation of moist static energy in updraft
 688 plume and in environment. $h = c_p T + gz + L_v q$ is the moist static energy in the en-
 689 vironment, and $h^* = c_p T + gz + L_v q^*$ is the saturation moist static energy in the up-
 690 draft plume. We specify radiative heating rate to be simply a function of temperature,

$$691 \quad Q_{rad}/(c_p \rho) = \begin{cases} Q_0, & \text{if } T > 250K \\ Q_0(0.5 + 0.5 \cos(\pi(250 - T)/(250 - 200))), & \text{if } 250K > T > 200K \\ 0, & \text{if } T < 200K \end{cases} \quad (\text{B13})$$

693 where $Q_0 = -1Kday^{-1}$. Radiative heating rate is constantly $-1Kday^{-1}$ in lower and
 694 middle troposphere and gradually decays to 0 from $T=250K$ to $T=200K$. $\rho = p/R_d T$
 695 is the air density.

696 Equation B7 implies the zero-buoyancy assumption that the temperature in up-
 697 drafts is the same as the temperature in the environment at the same height. Equation
 698 B8 is the parameterization of cloud evaporation in the environment, following the def-
 699 inition in the Singh and Neogi (2022). μ is a unitless parameter which controls the speed
 700 of cloud evaporation. We assume cloud evaporation happens at the level where cloud is

701 condensed, and we assume there is no evaporation of precipitation. Equation B9 is the
702 hydrostatic balance, and $R_d = 287 J kg^{-1} K^{-1}$ is the gas constant for dry air.

703 For Equation B1 to B9, there are 9 equations but 11 unknown variables: M_c , M_e ,
704 ϵ , δ , q^* , q , h , s_{cond} , s_{evap} , μ , and p . We have excluded h^* and Q_{rad} from unknown vari-
705 ables since they can be expressed using h^* and p through Equation B12 and B13. We
706 take ϵ and μ to be the free parameters that we can specify, and the rest of the equations
707 is just enough to get self-consistent solution. If one further specifies δ , then there will
708 be more equations than unknown variables, in which case there cannot be self-consistent
709 solution. Next, we will describe how we solve these equations as an ODE problem and
710 express the equations as $\frac{\partial}{\partial z}(M_c, p, q, T) = F(M_c, p, q, T)$.

711 Replacing Equation B1 into Equation B3 to B7, we can get:

$$712 \quad M_c \frac{\partial q^*}{\partial z} = -\epsilon(1 - RH)M_c q^* - s_{cond} \quad (B14)$$

$$713 \quad M_e \frac{\partial q}{\partial z} = \delta(1 + \mu)(1 - RH)M_c q^* \quad (B15)$$

$$714 \quad M_c \frac{\partial h^*}{\partial z} = -\epsilon L_v(1 - RH)M_c q^* \quad (B16)$$

$$715 \quad M_e \frac{\partial h}{\partial z} = \delta L_v(1 - RH)M_c q^* + Q_{rad} \quad (B17)$$

717 $RH = q/q^*$ is the relative humidity in the environment.

718 Equation B1 can be rewritten as:

$$719 \quad \frac{\partial M_c}{\partial z} = M_c(\epsilon - \delta) \quad (B18)$$

721 Using Equation B2 and B15, we get:

$$722 \quad \frac{\partial q}{\partial z} = -\delta(1 + \mu)(1 - RH)q^* \quad (B19)$$

724 Equation B16 can be used to express the temperature lapse rate $\Gamma = -\frac{\partial T}{\partial z}$. From
725 the definition of h^* , we have:

$$726 \quad \frac{\partial h^*}{\partial z} = -c_p \Gamma + g + L_v \frac{\partial q^*}{\partial z} \quad (B20)$$

728 Using Equation B9 and B12 and defining $\gamma = -(1/q^*)\frac{\partial q^*}{\partial z}$, we can get:

$$729 \quad \gamma = \frac{L_v \Gamma}{R_v T^2} - \frac{g}{R_d T} \quad (B21)$$

731 Replacing Equation B20 and B21 into Equation B16, we can get:

$$732 \quad \frac{\partial T}{\partial z} = \frac{1}{c_p + q^* L_v^2 / (R_v T^2)} [-g(1 + \frac{L_v q^*}{R_d T}) - \epsilon L_v(1 - RH)q^*] \quad (B22)$$

734 When we sum Equation B3 and B4, sum Equation B5 and B6, and use Equation
735 B2 and B7, we can get the energy balance equation:

$$736 \quad Q_{rad} = L_v(s_{cond} - s_{evap}) \quad (B23)$$

738 Replacing Equation B8 and B14 into Equation B23, we can get the expression of
739 M_c or δ :

$$740 \quad M_c = -\frac{Q_{rad}/(L_v q^*)}{\gamma - (\epsilon + \mu\delta)(1 - RH)} \quad (B24)$$

$$741 \quad \delta = -\frac{\epsilon}{\mu} + \frac{\gamma}{\mu(1 - RH)} + \frac{Q_{rad}}{\mu(1 - RH)q^* L_v M_c} \quad (B25)$$

743 Now with Equation B9, B18, B19, B22, and B25, we have the closed form expres-
 744 sion for our ODE problem:

$$745 \frac{\partial}{\partial z}(M_c, p, q, T) = F(M_c, p, q, T) \quad (B26)$$

747 where the right hand side only depends on M_c , p , q , and T . Given boundary conditions
 748 at cloud base (we use $z=500\text{m}$), Equation B26 can integrate upwards and get the full
 749 atmosphere profiles.

750 For boundary conditions, we specify a surface temperature of 303K and surface pres-
 751 sure of 10^5 Pa. We assume dry adiabatic lapse rate of $g/c_p = 9.8\text{Kkm}^{-1}$ below cloud
 752 base, and we can use Equation B9 to integrate pressure p from the surface to cloud base.
 753 For environmental water vapor mixing ratio q at cloud base, we do not have a solid con-
 754 strain. If one assumes $\frac{\partial q}{\partial z} \approx RH \frac{\partial q^*}{\partial z}$ (the vertical gradient of RH is much smaller than
 755 the vertical gradient of q^*), Equation B15 can reduce to:

$$756 RH = \frac{\delta(1 + \mu)}{\delta(1 + \mu) + \gamma} \quad (B27)$$

758 We determine our cloud base q using Equation B27, and the value of δ in Equation B27
 759 is taken from the ϵ . In this way, we implicitly assumes that increasing ϵ or μ can have
 760 a moistening effect at the cloud base, which intuitively makes sense. We will show later
 761 the sensitivity of solution to the value of cloud base q .

762 For M_c , we do not have a direct cloud base constrain. However, we assume our so-
 763 lution is in radiative-convective equilibrium (RCE), which says radiative cooling must
 764 be balanced by latent heat release at all the levels. The RCE condition requires that M_c
 765 reaches 0 exactly at the level where the radiative cooling rate becomes 0, i.e., at $T=200\text{K}$
 766 (Equation B13). If cloud base M_c is too large, M_c will still be positive where $T=200\text{K}$.
 767 If cloud base M_c is too small, M_c will go to 0 before radiative cooling decays to 0. We
 768 can have a random initial guess of cloud base M_c and change our guess based on this RCE
 769 condition. Once we find lower and upper bounds of the cloud base M_c , we use binary
 770 search to iteratively guess between the bounds and narrow the bounds until we find the
 771 M_c that satisfies the RCE condition.

772 In Fig. B1 we test the sensitivity of the atmospheric profiles to the cloud base wa-
 773 ter vapor mixing ratio (or equivalently RH). We change the cloud base RH from 70%
 774 to 90%. Except temperature profile, the influence of cloud base RH on other variables
 775 is primarily within the lower 5km and does not have a big impact to the upper tropo-
 776 sphere. The temperature becomes warmer through the whole troposphere with moister
 777 cloud base environment. For cloud base mass flux, it strongly depends on the RH based
 778 on Equation 5 in the main text. The way we determine the cloud base RH using Equa-
 779 tion B27 will implicitly lead to the sensitivity that cloud base mass flux increases when
 780 ϵ or μ increase. Since our main focus in this paper is the upper troposphere mass flux,
 781 the uncertainty in how we determine the cloud base RH will likely not change our re-
 782 sults. We also tested fixing the relative humidity at the cloud base. The sensitivities re-
 783 garding to mixing strength and evaporation rate remain qualitatively the same. In fu-
 784 ture research, it would be beneficial to integrate considerations of energy and water con-
 785 servation in the subcloud layer, along with surface flux parameterization, to automat-
 786 ically determine the cloud base relative humidity.

787 In Fig. B2 we test the sensitivity to different sea surface temperature. We can see
 788 that the whole troposphere becomes higher with the profiles of most quantities shifting
 789 upwards. The peak value of mass flux near the anvil level decreases with warmer sur-
 790 face temperature, which will indicate a weaker mass detrainment and likely a decrease
 791 of anvil cloud fraction (if lifetime is assumed to be unchanged with surface warming).
 792 The decrease of upper troposphere mass flux is consistent with the stability iris effect
 793 proposed in (Bony et al., 2016).

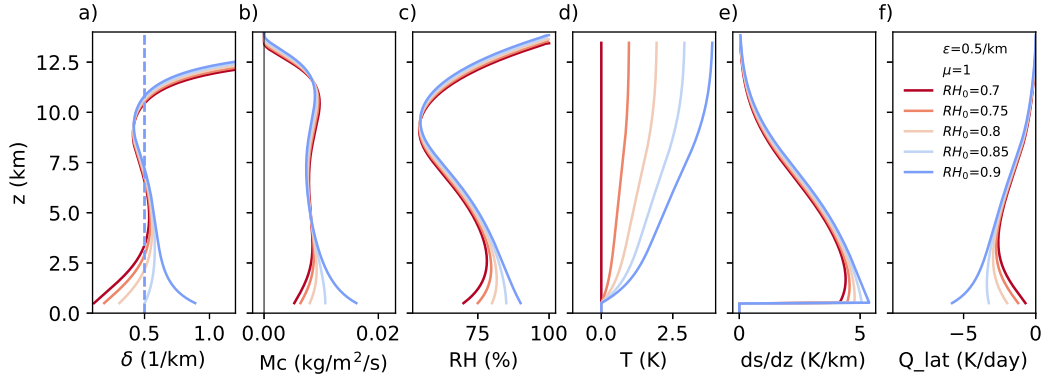


Figure B1. Atmosphere profiles in the zero-buoyancy plume model with varying cloud-base relative humidity (blue color represents more moist environment), entrainment rate $\epsilon = 0.5 \text{ km}^{-1}$, and cloud evaporation parameter $\mu = 1$. The variables shown are detrainment rate (a), updraft mass flux (b), relative humidity (c), temperature (d), vertical gradient of dry static energy (e), and latent heating rate due to cloud evaporation in the environment (f). Dashed lines in panel a are the profiles of prescribed entrainment rate. The temperature in panel d is shown as deviation to one of the simulations, which is denoted by the red line with zero deviation.

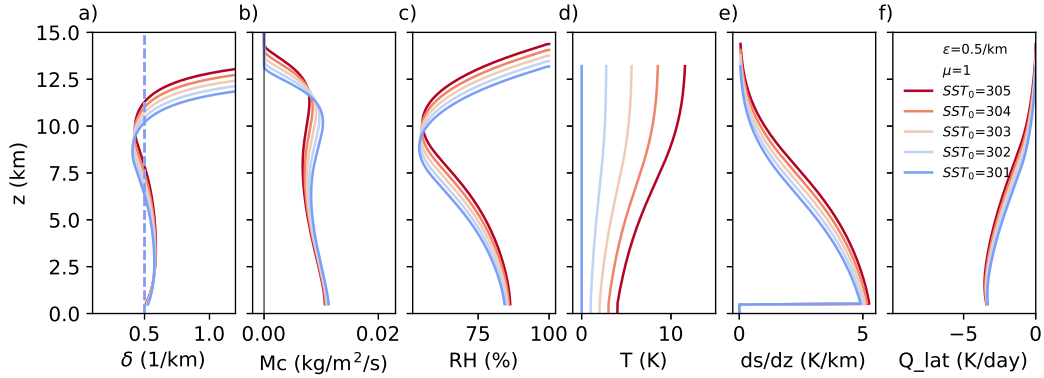


Figure B2. Similar to Fig. B1 but with sea surface temperature (blue color represents colder surface temperature), entrainment rate $\epsilon = 0.5 \text{ km}^{-1}$, and cloud evaporation parameter $\mu = 1$.

Acknowledgments

We thank Marat Khairoutdinov for making the SAM model available. ZH thanks Peter Blossey, Blaž Gasparini, Chris Bretherton, and Andrea Jenney for discussion/comments on this work. ZH and ZK acknowledge the funding from NSF Grant 1743753 and from the Office of Biological and Environmental Research of the U.S. DOE under grant DE-SC0022887 as part of the ASR Program. ZH acknowledges Grant DGE1745303 from NSF Graduate Research Fellowships Program.

References

- Becker, T., Stevens, B., & Hohenegger, C. (2017). Imprint of the convective parameterization and sea-surface temperature on large-scale convective self-aggregation. *Journal of Advances in Modeling Earth Systems*, *9*(2), 1488–1505.
- Beydoun, H., Caldwell, P. M., Hannah, W. M., & Donahue, A. S. (2021). Dissecting anvil cloud response to sea surface warming. *Geophysical Research Letters*, *48*(15), e2021GL094049.
- Bogenschutz, P. A., Eldred, C., & Caldwell, P. M. (2023). Horizontal resolution sensitivity of the simple convection-permitting e3sm atmosphere model in a doubly-periodic configuration. *Journal of Advances in Modeling Earth Systems*, *15*(7), e2022MS003466. Retrieved from <https://agupubs.onlinelibrary.wiley.com/doi/abs/10.1029/2022MS003466> (e2022MS003466 2022MS003466) doi: <https://doi.org/10.1029/2022MS003466>
- Bony, S., Stevens, B., Coppin, D., Becker, T., Reed, K. A., Voigt, A., & Medeiros, B. (2016). Thermodynamic control of anvil cloud amount. *Proceedings of the National Academy of Sciences*, *113*(32), 8927–8932.
- Bony, S., Stevens, B., Frierson, D. M., Jakob, C., Kageyama, M., Pincus, R., . . . others (2015). Clouds, circulation and climate sensitivity. *Nature Geoscience*, *8*(4), 261–268.
- Bretherton, C. S., McCaa, J. R., & Grenier, H. (2004). A new parameterization for shallow cumulus convection and its application to marine subtropical cloud-topped boundary layers. part i: Description and 1d results. *Monthly weather review*, *132*(4), 864–882.
- Bryan, G. H., Wyngaard, J. C., & Fritsch, J. M. (2003). Resolution requirements for the simulation of deep moist convection. *Monthly Weather Review*, *131*(10), 2394–2416.
- Hartmann, D. L., Gasparini, B., Berry, S. E., & Blossey, P. N. (2018). The life cycle and net radiative effect of tropical anvil clouds. *Journal of Advances in Modeling Earth Systems*, *10*(12), 3012–3029.
- Hohenegger, C., Kornblueh, L., Klocke, D., Becker, T., Cioni, G., Engels, J. F., . . . Stevens, B. (2020). Climate statistics in global simulations of the atmosphere, from 80 to 2.5 km grid spacing. *Journal of the Meteorological Society of Japan. Ser. II*, *98*(1), 73–91.
- Hu, Z., Jeevanjee, N., & Kuang, Z. (2023). From grid to cloud: Understanding the impact of grid size on simulated anvil clouds and atmospheric profiles [software]. doi: <https://doi.org/10.5281/zenodo.8397768>
- Hu, Z., Lamraoui, F., & Kuang, Z. (2021). Influence of upper-troposphere stratification and cloud–radiation interaction on convective overshoots in the tropical tropopause layer. *Journal of the Atmospheric Sciences*, *78*(8), 2493–2509.
- Iacono, M. J., Delamere, J. S., Mlawer, E. J., Shephard, M. W., Clough, S. A., & Collins, W. D. (2008). Radiative forcing by long-lived greenhouse gases: Calculations with the aer radiative transfer models. *Journal of Geophysical Research: Atmospheres*, *113*(D13).

- 847 Jeevanjee, N. (2017). Vertical velocity in the gray zone. *Journal of Advances in*
848 *Modeling Earth Systems*, 9(6), 2304–2316.
- 849 Jeevanjee, N. (2022). Three rules for the decrease of tropical convection with
850 global warming. *Journal of Advances in Modeling Earth Systems*, 14(11),
851 e2022MS003285.
- 852 Jeevanjee, N., & Zhou, L. (2022). On the resolution-dependence of anvil cloud frac-
853 tion and precipitation efficiency in radiative-convective equilibrium. *Journal of*
854 *Advances in Modeling Earth Systems*, 14(3), e2021MS002759.
- 855 Khairoutdinov, M. (2023). System for atmospheric modeling [software]. Retrieved
856 from <http://rossby.msrc.sunysb.edu/~marat/SAM/>
- 857 Khairoutdinov, M., Krueger, S. K., Moeng, C.-H., Bogenschutz, P. A., & Randall,
858 D. A. (2009). Large-eddy simulation of maritime deep tropical convection.
859 *Journal of Advances in Modeling Earth Systems*, 1(4).
- 860 Khairoutdinov, M., & Randall, D. A. (2003). Cloud resolving modeling of the arm
861 summer 1997 iop: Model formulation, results, uncertainties, and sensitivities.
862 *Journal of the Atmospheric Sciences*, 60(4), 607–625.
- 863 Kuang, Z., & Bretherton, C. S. (2006). A mass-flux scheme view of a high-resolution
864 simulation of a transition from shallow to deep cumulus convection. *Journal of*
865 *the Atmospheric Sciences*, 63(7), 1895–1909.
- 866 Miyamoto, Y., Kajikawa, Y., Yoshida, R., Yamaura, T., Yashiro, H., & Tomita, H.
867 (2013). Deep moist atmospheric convection in a subkilometer global simula-
868 tion. *Geophysical Research Letters*, 40(18), 4922–4926.
- 869 Morrison, H., Curry, J., & Khvorostyanov, V. (2005). A new double-moment micro-
870 physics parameterization for application in cloud and climate models. part i:
871 Description. *Journal of the atmospheric sciences*, 62(6), 1665–1677.
- 872 Powell, S. W., Houze, R. A., Kumar, A., & McFarlane, S. A. (2012). Comparison
873 of simulated and observed continental tropical anvil clouds and their radiative
874 heating profiles. *Journal of the Atmospheric Sciences*, 69(9), 2662–2681.
- 875 Romps, D. M. (2014). An analytical model for tropical relative humidity. *Journal of*
876 *Climate*, 27(19), 7432–7449.
- 877 Romps, D. M. (2021). Ascending columns, wtg, and convective aggregation. *Journal*
878 *of the Atmospheric Sciences*, 78(2), 497–508.
- 879 Satoh, M., Stevens, B., Judt, F., Khairoutdinov, M., Lin, S.-J., Putman, W. M., &
880 Düben, P. (2019). Global cloud-resolving models. *Current Climate Change*
881 *Reports*, 5, 172–184.
- 882 Seeley, J. T., Jeevanjee, N., Langhans, W., & Romps, D. M. (2019). Formation of
883 tropical anvil clouds by slow evaporation. *Geophysical Research Letters*, 46(1),
884 492–501.
- 885 Sherwood, S., Webb, M. J., Annan, J. D., Armour, K. C., Forster, P. M., Harg-
886 reaves, J. C., . . . others (2020). An assessment of earth’s climate sensitivity us-
887 ing multiple lines of evidence. *Reviews of Geophysics*, 58(4), e2019RG000678.
- 888 Siebesma, A., & Jonker, H. (2000). Anomalous scaling of cumulus cloud boundaries.
889 *Physical review letters*, 85(1), 214.
- 890 Singh, M. S., & Neogi, S. (2022). On the interaction between moist convection and
891 large-scale ascent in the tropics. *Journal of Climate*, 35(14), 4417–4435.
- 892 Singh, M. S., & O’Gorman, P. A. (2013). Influence of entrainment on the ther-
893 mal stratification in simulations of radiative-convective equilibrium. *Geophysi-
894 cal Research Letters*, 40(16), 4398–4403.
- 895 Singh, M. S., Warren, R. A., & Jakob, C. (2019). A steady-state model for the rela-
896 tionship between humidity, instability, and precipitation in the tropics. *Journal*
897 *of Advances in Modeling Earth Systems*, 11(12), 3973–3994.
- 898 Stevens, B., Satoh, M., Auger, L., Biercamp, J., Bretherton, C. S., Chen, X., . . .
899 others (2019). Dyamond: the dynamics of the atmospheric general circula-
900 tion modeled on non-hydrostatic domains. *Progress in Earth and Planetary*
901 *Science*, 6(1), 1–17.

- 902 Wing, A. A., Stauffer, C. L., Becker, T., Reed, K. A., Ahn, M.-S., Arnold, N. P.,
903 ... others (2020). Clouds and convective self-aggregation in a multimodel
904 ensemble of radiative-convective equilibrium simulations. *Journal of Advances*
905 *in Modeling Earth Systems*, 12(9), e2020MS002138.
- 906 Zelinka, M. D., Myers, T. A., McCoy, D. T., Po-Chedley, S., Caldwell, P. M., Ceppi,
907 P., ... Taylor, K. E. (2020). Causes of higher climate sensitivity in cmip6
908 models. *Geophysical Research Letters*, 47(1), e2019GL085782.

1 **From Grid to Cloud: Understanding the Impact of**
2 **Grid Size on Simulated Anvil Clouds and Atmospheric**
3 **Profiles**

4 **Zeyuan Hu¹, Nadir Jeevanjee², Zhiming Kuang^{1,3}**

5 ¹Department of Earth and Planetary Sciences, Harvard University, Cambridge, MA, USA

6 ²Geophysical Fluid Dynamics Laboratory, Princeton, NJ, USA

7 ³John A. Paulson School of Engineering and Applied Sciences, Harvard University, Cambridge, MA, USA

8 **Key Points:**

- 9 • We found a resolution dependence of anvil cloud fraction and updraft mass flux
10 in simulations mostly due to the change of cloud-air mixing.
11 • We derived a self-consistent solution for a zero-buoyancy plume model as a sim-
12 ple tool to understand steady-state tropical atmosphere.
13 • We observed a convergence in atmospheric profiles, including anvil cloud fraction,
14 at a grid resolution of approximately 100m.

Corresponding author: Zeyuan Hu, zeyuan.hu@fas.harvard.edu

Abstract

In this study, we explore the relationship between anvil cloud fraction and horizontal model resolution in small domain radiative-convective equilibrium (RCE) simulations, building on the findings of Jeevanjee and Zhou (2022). Using the System of Atmosphere Modeling (SAM) model, we find that finer resolutions yield higher anvil cloud fractions due to larger convective updrafts mass flux and increased mass detrainment at anvil levels. Employing two different microphysics schemes, we illustrate that finer resolution can enhance mass flux through either stronger cloud evaporation or weaker upper-troposphere stability, as the consequence of enhanced horizontal mixing. Moreover, we refine an analytical zero-buoyancy plume model to investigate the effects of adjusting entrainment rate and evaporation rate on vertical atmosphere profiles in a simple theoretical framework. Our solutions of the zero-buoyancy plume model suggest that stronger horizontal mixing can lead to larger convective updraft mass flux, consistent with the analysis in numerical simulations. We also observe the likelihood of atmospheric profiles converging at a grid size of approximately 100m, potentially as a result of converging entrainment rate and mixing strength. These insights have implications for global storm-resolving simulations, implying a possible convergence of high cloud and deep convection properties as the horizontal resolution approaches around 100m.

Plain Language Summary

High, anvil-shaped clouds in the tropics significantly impact our climate, but simulating them accurately is challenging. Our study reveals that the area these clouds cover in simplified simulations is largely affected by the level of detail in representing the tropical atmosphere. As we refine the simulation resolution, cloud evaporation and the rate of mixing between cloudy and clear air (entrainment) increase, leading to more vigorous updrafts and higher upward mass transport at the level of these high clouds. Consequently, we observe more coverage of high clouds as the simulation resolution improves. Our research indicates that to achieve more realistic cloud simulations, we need to factor in how these processes change with resolution. We expect that the properties of these clouds will begin to converge in the simulations when the grid size reaches approximately the order of 100m.

1 Introduction

Simulating cloud and convection accurately has long been a major challenge for accurate climate and weather simulations. Uncertainty associated with cloud remains as one of the most significant factors contributing to climate feedback uncertainties in future climate change projections (e.g., Bony et al., 2015; Zelinka et al., 2020). In recent years, the scientific community has made significant strides in developing and examining global storm-resolving models (GSRM) with grid sizes of 1-5km (e.g., Satoh et al., 2019; Stevens et al., 2019). By explicitly resolving deep convection, GSRMs can bypass the uncertainties in convective parameterization. A crucial question for using the GSRMs is whether a resolution at the order of 1km is sufficient to resolve relevant atmospheric physical processes.

Resolution dependence in atmosphere models that explicitly resolve deep convection has been extensively studied in various simulation setup. By changing horizontal grid size from 80km to 2.5km in a GSRM, Hohenegger et al. (2020) showed that many 40-day mean, global mean climate statistics, such as precipitation, sensible heat flux, and outgoing longwave radiation, exhibit weak resolution dependence compared with the uncertainties across different GSRMs. However, Hohenegger et al. (2020) also showed some convection and cloud properties, such as the width of the Intertropical Convergence Zone and the fraction of deep convective clouds, have not converged even at 2.5km resolution. Miyamoto et al. (2013) also examined the sensitivity of deep convection to resolution at

65 around the order of 1km in global simulations. They showed that deep convective cores
 66 start to occupy more than one grid point at around 2km and have stronger upward ve-
 67 locity with finer resolution. In idealized squall line simulations, Bryan et al. (2003) showed
 68 decreasing grid size from the order of 1km to the order of 100m tends to give more tur-
 69 bulent flow with resolved entrainment and overturning within clouds. In limited-area 24-
 70 hour simulations with tropical maritime large-scale forcing, Khairoutdinov et al. (2009)
 71 found low sensitivity of quantities such as cloud fraction, relative humidity, and precip-
 72 itation rate to grid size ranging from 100m to 1600m, but updraft core statistics are sen-
 73 sitive to resolution, with finer resolution showing larger upward velocity and more total
 74 water in updraft core. From limited-area radiative-convective equilibrium (RCE) sim-
 75 ulation studies, Jeevanjee (2017) showed that the updraft velocity can keep increasing
 76 with finer resolution until grid size is at the order of 100m. Jeevanjee and Zhou (2022)
 77 found that, in RCE simulation, high cloud fraction exhibits strong resolution dependence,
 78 with finer resolution leading to higher anvil cloud fraction.

79 In the present study, we focus on the resolution dependence of anvil cloud fraction
 80 in RCE simulations. Anvil cloud plays a crucial role in regulating the atmospheric ra-
 81 diation flux, but large uncertainties remain in the modeling of anvil clouds. In a study
 82 from an intermodel comparison project of RCE simulations (Wing et al., 2020), even un-
 83 der very similar setups, different models produce very different anvil cloud fraction and
 84 disagree on the sign of anvil cloud fraction change with warmer sea surface temperature.
 85 Sherwood et al. (2020) reported that cloud feedback uncertainty associated with anvil
 86 clouds is comparable to other types of clouds such as tropical marine low clouds. Anvil
 87 cloud fraction could be thought of as the product of mass detrainment and lifetime of
 88 detrained clouds (e.g., Seeley et al., 2019; Beydoun et al., 2021). The mass detrainment
 89 describes how fast cloud mass is ejected into the atmosphere from deep convective core.
 90 The mass detrainment is closely related to the mass flux of convective updrafts reach-
 91 ing the upper troposphere. The lifetime describes how long the detrained cloud mass can
 92 stay in the atmosphere before removed by evaporation/sublimation and sedimentation.
 93 The lifetime can be sensitive to microphysics parameterization used in the model (e.g.,
 94 Hartmann et al., 2018). Different microphysics schemes can lead to very different anvil
 95 cloud fraction (e.g., see our results in later sections).

96 Jeevanjee and Zhou (2022) (hereafter, JZ22) showed a striking dependence of anvil
 97 cloud fraction on horizontal resolution. In their simulations, they observed that the peak
 98 anvil cloud fraction rises dramatically from approximately 5% at the coarsest 16 km grid
 99 size to over 40% at the finest 62.5 m resolution, with no indication of convergence even
 100 at this highest resolution. They argued that finer horizontal resolution corresponds to
 101 stronger mixing with a shorter mixing timescale, which they defined as the time for a
 102 cloudy grid to completely mixed with a neighboring clear grid. The stronger mixing can
 103 enhance cloud evaporation and lower precipitation efficiency. A smaller precipitation ef-
 104 ficiency would then lead to greater cloud based mass flux, which would lead to more mass
 105 flux reaching upper troposphere and producing more anvil clouds.

106 While the findings in JZ22 offer significant insights, it is intriguing to note the dif-
 107 fering results presented by Bogenschutz et al. (2023). Specifically, they observed that dur-
 108 ing a 20-day simulation with observed large-scale forcing, the anvil cloud fraction is in-
 109 sensitive when the resolution changes from 5km to 500m, whereas in JZ22 the anvil cloud
 110 fraction does not converge even at a grid size of 62.5m. The duration of the simulation
 111 and the presence or absence of large-scale forcing could be influential factors. Notably,
 112 JZ22 ran simulations over a longer period (50 days) to achieve radiative-convective equi-
 113 librium, without including any large-scale forcing. Furthermore, differences in microphysics
 114 and sub-grid turbulence parameterization used in the two studies might also contribute
 115 to the different sensitivity of high clouds.

116 In this study, we would like to further examine the causality in the argument in
 117 JZ22 that enhanced mixing with finer resolution can lead to more convective updraft mass

118 flux in the upper troposphere through increased precipitation efficiency and increased
 119 cloud base mass flux. Jeevanjee (2022) showed that the increase in cloud base mass flux
 120 due to higher precipitation efficiency is not entirely robust, given the unconstrained ef-
 121 fects of entrainment and detrainment. It is also not clear whether changes in cloud base
 122 mass flux can consistently project to the upper troposphere, again considering the un-
 123 constrained effects of entrainment and detrainment.

124 We tested the resolution dependence of anvil cloud fraction in small-domain RCE
 125 simulations with grid size ranging from 4km to 125m. The domain size is fixed across
 126 different simulations. Since the anvil cloud fraction is sensitive to microphysics param-
 127 eterization, we examined the mechanism for the resolution dependence in two different
 128 microphysics schemes. We found that anvil cloud fraction shows sign of convergence when
 129 the grid size is at the order of 100m. Consistent with JZ22, due to enhanced horizon-
 130 tal mixing, finer resolution produces more updraft mass flux in the upper troposphere
 131 and leads to increasing anvil cloud fraction. The stronger mixing in finer resolution leads
 132 to enhanced cloud evaporation and stronger entrainment rate. By examining the clear-
 133 sky energy budgets, we showed that both the enhanced cloud evaporation and the stronger
 134 entrainment rate could contribute to a stronger environmental subsidence and updraft
 135 mass flux.

136 We further used an analytical zero-buoyancy plume model to examine the effects
 137 of changing evaporation rate and entrainment rate in a simple theoretical framework.
 138 We refined the plume model and derived self-consistent solutions of RCE atmosphere pro-
 139 files. We found that increasing entrainment rate can lead to increase of upper troposphere
 140 mass flux through either more cloud evaporation or weaker stability in the upper tro-
 141 posphere. However, increasing evaporation rate alone may not necessarily change the up-
 142 draft mass flux in the upper troposphere. The insights from the analytical plume model
 143 emphasize the role of the horizontal mixing and refine the pathway connecting enhanced
 144 mixing to a stronger upper tropospheric mass flux.

145 The rest of the manuscript is structured as follow: in section 2 we describe the ex-
 146 perimental setup. Section 3 shows our results. Section 3.1 shows the contribution of mass
 147 detrainment and lifetime to the cloud fraction changes. Section 3.2 shows how the stronger
 148 mixing in finer resolution simulations contributes to more updraft mass flux through en-
 149 ergy balance. Section 3.3 shows the results and insights from the analytical solution of
 150 the zero-buoyancy plume model. Section 4 is the discussion and summary.

151 2 Experiment setup

152 We use the System for Atmosphere Modeling (SAM; Khairoutdinov & Randall, 2003),
 153 version 6.10.6, configured as a cloud-resolving model. We run three-dimensional RCE
 154 simulations using the same domain size of 128km×128km with different horizontal res-
 155 olution of 4km, 2km, 1km, 500m, 250m, and 125m. All simulations use 60 vertical lev-
 156 els with model top located at 26km and a rigid-lid top boundary condition. The verti-
 157 cal grid spacing increases from 75m near the surface to a constant of 500m through the
 158 whole free troposphere and above. A sponge layer is located in the upper 30% of the model
 159 domain (i.e., above 18km). The radiation scheme is Rapid and Accurate Radiative Trans-
 160 fer Model for General Circulation Models (RRTMG) (Iacono et al., 2008). A simple Smagorinsky-
 161 type scheme (Khairoutdinov & Randall, 2003) is used for the effect of subgrid-scale mo-
 162 tion. We use a constant solar insolation (no diurnal cycle) with fixed solar constant of
 163 683.5 W m^{-2} and zenith angle of 50.5° . Domain-averaged horizontal wind is nudged to
 164 zero at each vertical level with a nudging time scale of 1hour. Sea surface temperature
 165 is fixed uniformly at 303K.

166 We use two different microphysics schemes: SAM single-moment scheme (SAM1MOM,
 167 Khairoutdinov & Randall, 2003) and a double-moment Morrison scheme (Morrison et

168 al., 2005). The SAM one-moment scheme uses an instantaneous saturation adjustment
 169 to generate and remove cloud condensate. Between 0° and -20°C, partitioning of cloud
 170 condensate into cloud ice and liquid water depends linearly on temperature (at -20°C,
 171 all condensate is ice; at 0°C, all condensate is liquid water). More pathways for conver-
 172 sion between different hydrometeors are included in the Morrison double-moment scheme.
 173 The Morrison scheme tends to produce more ice cloud in the upper troposphere (e.g.,
 174 Powell et al., 2012; Hu et al., 2021) and consequently strong atmospheric cloud radi-
 175 ative heating in the middle and upper troposphere. This stronger atmospheric cloud ra-
 176 diative heating can stabilize the upper troposphere and weaken the convective updraft
 177 reaching the upper troposphere (Hu et al., 2021). As we will show later, the weaker up-
 178 per troposphere mass flux will lead to less cloud evaporation in the environment in the
 179 Morrison scheme than in the SAM1MOM scheme.

180 For the simulations with horizontal resolution from 4km to 250m, the first 50 days
 181 are taken as the model spinup and considered long enough for the model to reach equi-
 182 librium. After the 50-day spinup, a 20-day post-equilibrium period is used for analysis.
 183 The 30 samples-per-hour data are then averaged to get an hourly output of domain-mean
 184 statistics. For the 125m-resolution simulation, we initialize the simulation with the equilib-
 185 rium temperature and moisture profile from the 500m-resolution simulation. Then we run
 186 only 30 days for spinup and another 20 days for analysis.

187 3 Results

188 3.1 Cloud fraction change due to mass detrainment

189 Fig. 1 illustrates the resolution-dependent behavior of cloud fraction, atmospheric
 190 cloud radiative effects, and relative humidity. A grid is classified as cloudy if the cloud
 191 mass (the sum of ice and liquid water) mixing ratio exceeds 10^{-5} kg kg⁻¹. As the grid
 192 spacing decreases from 4km to 125m, the peak anvil cloud fraction increases from 7.5%
 193 to 13% in the SAM1MOM simulations (Fig. 1a) and from 17% to 27% in the Morrison
 194 simulations (Fig. 1d). This amplified cloud fraction subsequently leads to increased cloud
 195 radiative heating throughout the majority of the free troposphere (Fig. 1b and 1e). The
 196 cloud fraction profiles appear to converge when the grid spacing falls below 250m in the
 197 SAM1MOM simulations. Along with the increase of the cloud fraction, both the SAM1MOM
 198 and Morrison simulations exhibit a rise in relative humidity throughout the entire free
 199 troposphere with finer resolution (Fig. 1c and 1f).

200 Anvil cloud fraction can be diagnosed as the product of mass detrainment and cloud
 201 lifetime (e.g., Seeley et al. 2019, Beydoun et al. 2022). In Fig. 2, we present profiles of
 202 convective updraft mass flux and in-cloud sedimentation rate to look at the change of
 203 mass detrainment and lifetime change. The convective updraft is characterized by grids
 204 with a vertical velocity greater than 1 m s^{-1} and a cloud mixing ratio exceeding 10^{-5}
 205 kg kg⁻¹. The in-cloud sedimentation rate is defined as q_{csed}/q_c averaged over cloudy
 206 grids, where q_c is the cloud mass (ice plus liquid water) mixing ratio and q_{csed} is the
 207 tendency of q_c due to sedimentation of cloud ice. This sedimentation rate is the major
 208 term of the net removal rate in Beydoun et al. 2022 and could be interpreted as one over
 209 lifetime. Sedimentation rate is positive above around 10 km and negative below, repre-
 210 senting cloud ice falling from detraining level downwards. In both the SAM1MOM and
 211 Morrison simulations, the convective updraft mass flux at above 11km increases with higher
 212 resolution, signifying an increased vertical mass convergence above this altitude. By mass
 213 continuity, the increase of vertical convective mass flux convergence corresponds to an
 214 increase of mass detrainment and an increase of horizontal mass convergence in clear-
 215 sky region. The convective updraft mass flux at middle and lower troposphere shows non-
 216 monotonic change. This is partly due to increased cloud radiative effects with finer res-
 217 olution, which may stabilize the middle troposphere. The sedimentation rate is weaker
 218 for finer resolutions in the SAM1MOM scheme but is slightly stronger in the Morrison

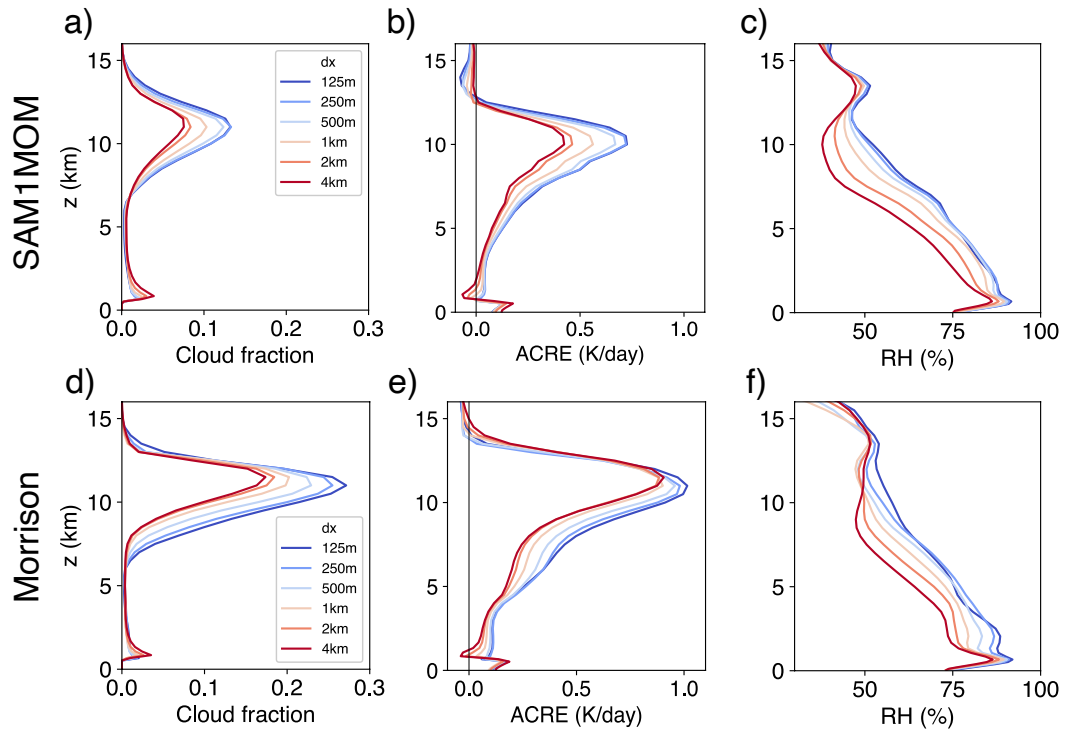


Figure 1. Domain-mean steady-state profiles of cloud fraction (left column), atmosphere cloud radiative effects (middle column) and relative humidity (right column). The upper row corresponds to the SAM1MOM simulations, while the lower row represents the Morrison simulations. Different colors indicate varying grid sizes, with warmer colors denoting coarser resolutions.

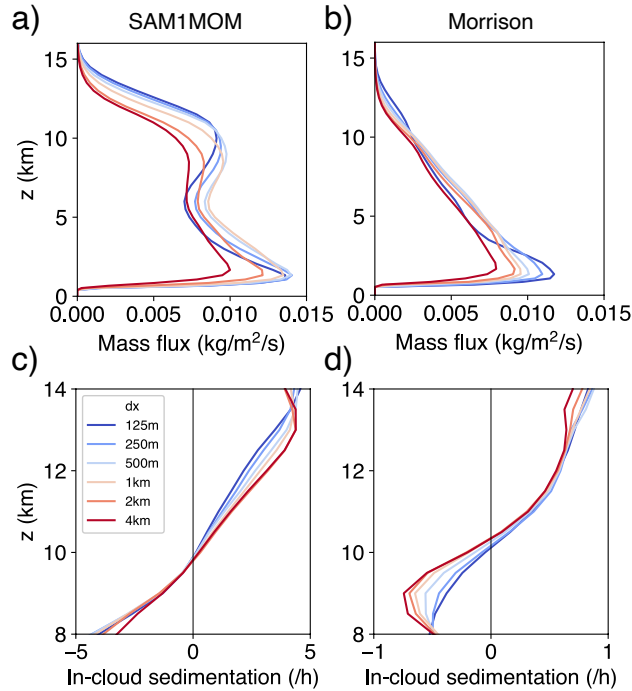


Figure 2. Domain-mean steady-state profiles of convective updraft mass flux (upper row) and cloud ice sedimentation rate (lower row). The left column corresponds to the SAM1MOM simulations, while the right column represents the Morrison simulations. Different colors indicate varying grid sizes, with warmer colors denoting coarser resolutions.

219 scheme. Hence, the observed increase in cloud fraction with finer resolution in both SAM1MOM
 220 and Morrison simulations is predominantly driven by the amplification of mass detrainment
 221 ment. The contribution from lifetime changes is less certain and could be contingent on
 222 the microphysics schemes employed.

223 3.2 Budgets for environmental subsidence

224 In this section, we investigate the mechanisms responsible for the increase in con-
 225 vective updraft mass flux associated with finer resolutions. According to the principle
 226 of mass continuity, the mass flux in convective updrafts must be balanced by subsidence
 227 in the surrounding environment, which we define as grids possessing a cloud mixing ratio
 228 less than $10^{-5} \text{ kg kg}^{-1}$. Consequently, elucidating changes in convective updrafts nec-
 229 cessitates a corresponding understanding of changes to environmental subsidence. By
 230 employing the dry static energy budget of the environment, we decompose the subsidence
 231 and will demonstrate that modifications to mass flux profiles could be attributed to changes
 232 in both cloud evaporation rate and entrainment rate. The changes in cloud evaporation
 233 and in entrainment rate are not purely independent as the change of horizontal mixing
 234 can influence both of them. The relative contribution of these two factors will be elab-
 235 orated upon in the subsequent section.

236 The dry static energy is defined as $s = c_p T + gz$. The conservation of dry static
 237 energy requires

$$238 \frac{\partial s}{\partial t} + \vec{u} \cdot \nabla_h s + w \frac{\partial s}{\partial z} = Q_{rad} + Q_{lat} \quad (1)$$

239 where Q_{rad} is radiative heating, and Q_{lat} is latent heating in the environment. By av-
 240 eraging over all environmental grids and time, and ignoring the time tendency, we obtain:
 241

$$242 \quad \langle \vec{u} \cdot \nabla_h s \rangle + \langle w \frac{\partial s}{\partial z} \rangle = \langle Q_{rad} \rangle + \langle Q_{lat} \rangle \quad (2)$$

243 After further decomposition of $\langle w \frac{\partial s}{\partial z} \rangle = \langle w \rangle \langle \frac{\partial s}{\partial z} \rangle + \langle w' \frac{\partial s'}{\partial z} \rangle$, the averaged environmen-
 244 tal subsidence can be expressed as:

$$245 \quad \langle w \rangle = \frac{\langle Q_{rad} \rangle}{\langle \frac{\partial s}{\partial z} \rangle} + \frac{\langle Q_{lat} \rangle}{\langle \frac{\partial s}{\partial z} \rangle} - \frac{\langle \vec{u} \cdot \nabla_h s \rangle}{\langle \frac{\partial s}{\partial z} \rangle} - \frac{\langle w' \frac{\partial s'}{\partial z} \rangle}{\langle \frac{\partial s}{\partial z} \rangle} \quad (3)$$

246 This equation essentially encapsulates the energy balance within the environment,
 247 implying that the subsidence heating is counterbalanced by the cooling induced by ra-
 248 diation and phase changes in water. In Fig. 3, we show the profiles of latent-driven and
 249 radiation-driven subsidence for the SAM1MOM simulations. The combined effect of latent-
 250 and radiation-driven subsidence closely mirrors the subsidence deduced from model out-
 251 put, and the contribution of advection terms appears minor in comparison to the con-
 252 tribution of radiation and latent heating (not shown).

253 The subsidence near anvil level increases with finer resolution (Fig. 3a), which is
 254 consistent with the change of convective updraft mass flux. In the SAM1MOM simula-
 255 tions, a large portion of the increasing subsidence is counteracted by the negative latent
 256 heating in the environment due to evaporation and sublimation of clouds (Fig. 3b). Con-
 257 versely, negative radiative heating accounts for a relatively smaller portion of this bal-
 258 ance (Fig. 3c). The relative contribution of latent and radiative heating in the Morri-
 259 son scheme is somewhat different. We will probe into the nuances of the Morrison sim-
 260 ulations later in this section. It is important to underscore that the role of latent heat-
 261 ing can be influenced by the specific definition of "environment". In our study, the en-
 262 vironment, defined as grids with a cloud mixing ratio less than $10^{-5} \text{ kg kg}^{-1}$, incorpo-
 263 rates grids distanced from clouds as well as those in close proximity to clouds, which ex-
 264 perience evaporation and sublimation from cloud. Results in the following paragraphs
 265 are not sensitive to the choice of cloud threshold. Changing the threshold from $10^{-5} \text{ kg kg}^{-1}$
 266 to $10^{-7} \text{ kg kg}^{-1}$ results in little change. Such insensitivity might be attributed to the model's
 267 procedural steps, wherein evaporation is calculated prior to the output of the cloud mix-
 268 ing ratio. Consequently, grid cells can reflect marginal cloud mixing ratios while still in-
 269 dicating evaporation in the resultant data.

270 The change of latent-driven subsidence is consistent with the change of latent heat-
 271 ing in the environment (Fig. 3d). In the upper troposphere the cooling from phase change
 272 is primarily associated with cloud evaporation/sublimation (Fig. 3e). For simplicity, we
 273 will henceforth use the term "evaporation" to refer to both the evaporation of cloud wa-
 274 ter and sublimation of cloud ice. The cooling due to re-evaporation of precipitation, which
 275 is not displayed here, is less significant than that of clouds in the upper troposphere, al-
 276 though it presents a similar strength in the lower troposphere. We have shown that a
 277 finer resolution model tends to generate more clouds and updraft mass flux. Therefore,
 278 the observed increase in latent cooling might be simply a consequence of the larger amount
 279 of clouds available for evaporation. However, an interesting observation arises when we
 280 normalize the cooling due to cloud evaporation by the domain mean cloud mass mix-
 281 ing ratio (Fig. 3f). Domain mean cloud mixing ratio is proportional to the total cloud
 282 mass in each layer. It becomes evident that, per unit mass, clouds tend to induce a greater
 283 amount of cooling in the environment in the upper troposphere (and also in lower alti-
 284 tudes) when modeled at finer resolution.

285 The observed enhancement in evaporation could be associated with the model res-
 286 olution through the geometric representation of cloud boundaries. We will use clouds at
 287 anvil level as an example, but we assume the intuition behind should apply to clouds at

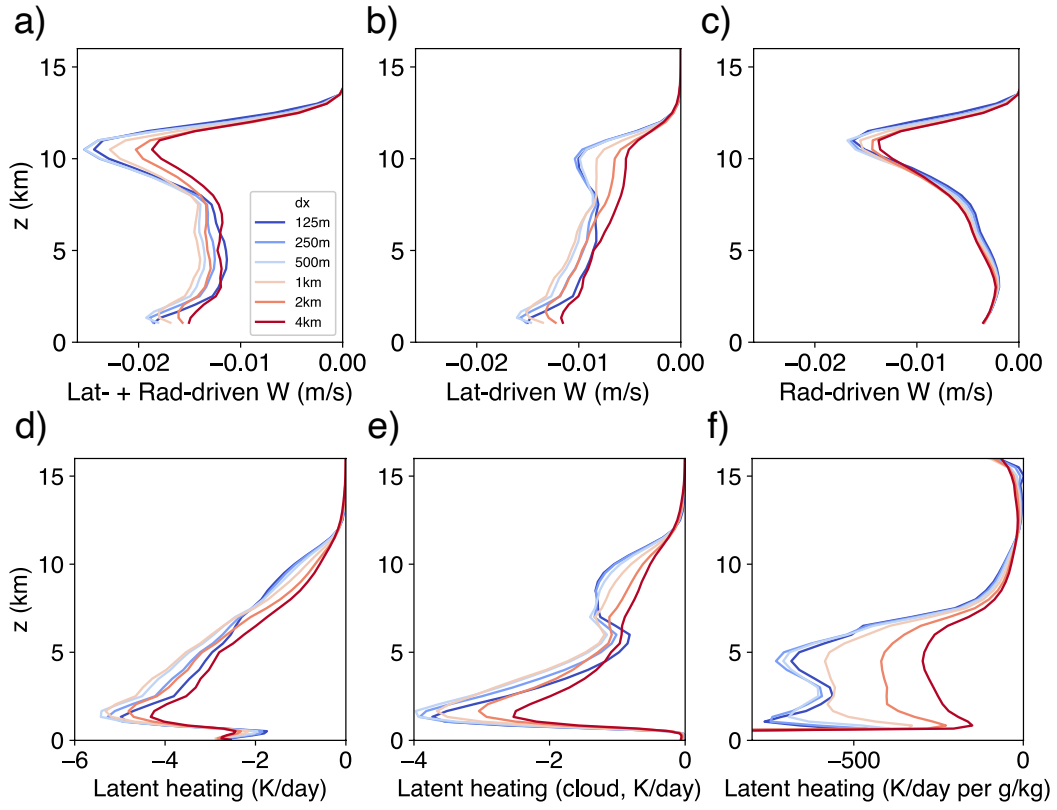


Figure 3. Energy budget for environmental subsidence for the SAM1MOM simulations. The first row shows the subsidence contributed by latent heat (panel b), by radiative cooling (panel c), and by both (a). Panel d shows the latent heating rate averaged in environments. Panel e shows the latent heating rate associated with the phase change between clouds and vapor averaged in environments. Panel f normalizes the cloud-related latent heating rate in panel e by the domain-mean cloud mixing ratio.

288 all the levels. Horizontal snapshots of the cloud mixing ratio at an altitude of $z=10\text{km}$
 289 are depicted in Fig. 4a and 4b. These images represent two $32\text{km}\times 32\text{km}$ subdomains
 290 in the 4km -resolution and 125m -resolution simulations respectively. When compared to
 291 the clouds in the coarser 4km -resolution simulation, the clouds in the 125m -resolution
 292 simulation exhibit more complex boundary structures and tend to be more dispersed.
 293 As a result, clouds modeled at finer resolutions exhibit a higher perimeter area ratio (Fig.
 294 4c). In other words, for a cloud patch of the same area, the total perimeter will be longer
 295 in the simulation with finer resolution. This effect is somewhat analogous to the coast-
 296 line paradox in fractal geometry, where the measured length of a coastline varies depend-
 297 ing on the scale of measurement. The increased perimeter to area ratio exposes a larger
 298 mass of the cloud to the environment, potentially leading to greater evaporation near
 299 the cloud edges.

300 The study by Siebesma and Jonker (2000) explored the fractal nature of cumulus
 301 clouds in Large-Eddy Simulations. They argued that while a coarse grid will underes-
 302 timate cloud surface area, the total sub-grid turbulent transport could become resolu-
 303 tion independent if the grid size is within the inertia subrange. However, in our simu-
 304 lations with a grid size on the order of 1km , sub-grid diffusion in the free troposphere
 305 is minimal. We observed that turning off horizontal sub-grid diffusion of scalars (such
 306 as energy and water) resulted in only minor changes to the profiles of cloud fraction and
 307 environmental evaporation (not shown). The cloud evaporation of deep convection is sub-
 308 stantially influenced by numerical diffusion and can be enhanced by a larger perimeter-
 309 to-area ratio. To illustrate this point, we derived an equation (see Appendix A for com-
 310 plete derivation) that describes the relationship between cloud evaporation in relation
 311 to resolved advection and the perimeter-to-area ratio:

$$312 \quad \frac{Q_{lat,env}}{q_m} = \frac{L}{A} U_{adv} \frac{q_{c,edge} + q_{v,env}^*(1 - RH)}{q_{cld}} \frac{L_v}{2c_p f_{env}} \quad (4)$$

313 The Equation 4 indicates that the evaporation due to horizontal mixing at cloud
 314 edges is dependent on several factors. These include the perimeter-to-area ratio (L/A),
 315 the resolved horizontal velocity near the cloud edge (U_{adv}), the cloud mixing ratio near
 316 the cloud edge ($q_{c,edge}$), the saturation deficit in the environment ($q_{v,env}^*(1 - RH)$), and
 317 the average cloud mixing ratio within cloudy grids (q_{cld}). We verify this equation at the
 318 anvil level, characterized by relatively weak vertical motion near the cloud edge, hence,
 319 making cloud evaporation predominantly attributable to horizontal mixing. Fig. 4d demon-
 320 strates that the diagnosed evaporation using Equation 4 qualitatively aligns with the di-
 321 rect model output. From this equation, it is evident that an increased perimeter to area
 322 ratio can positively contribute to enhanced cloud evaporation. In Appendix A, we delve
 323 into how other terms in Equation 4 vary with model resolution. It is more difficult to
 324 validate Equation 4 at lower levels. In the middle troposphere, clouds are typically very
 325 close to the convective core, and evaporation/condensation associated with vertical mo-
 326 tion may not be neglected. However, we assume the enhanced horizontal mixing and larger
 327 perimeter area ratio should still positively contribute to the enhanced evaporation we
 328 show in Fig. 3f. It is important to note the importance of enhanced horizontal mixing
 329 occurring at all levels, not solely at the anvil level. More efficient evaporation at lower
 330 levels could contribute to mass flux increase at those levels and, by mass continuity, should
 331 have a continuing influence on mass flux at higher levels.

332 In the Morrison simulations, we also observe an enhancement in subsidence near
 333 the anvil level, as shown in Fig. 5a. However, the contribution from latent-driven sub-
 334 sidence (Fig. 5b) is weaker in the Morrison scheme compared to the SAM1MOM scheme.
 335 Primarily, the subsidence change near anvil level is dominated by radiation-driven sub-
 336 sidence (see Fig. 5c). We will discuss more on the reasons for the diminished latent-driven
 337 subsidence near anvil level in the Morrison simulations at the end of this section.

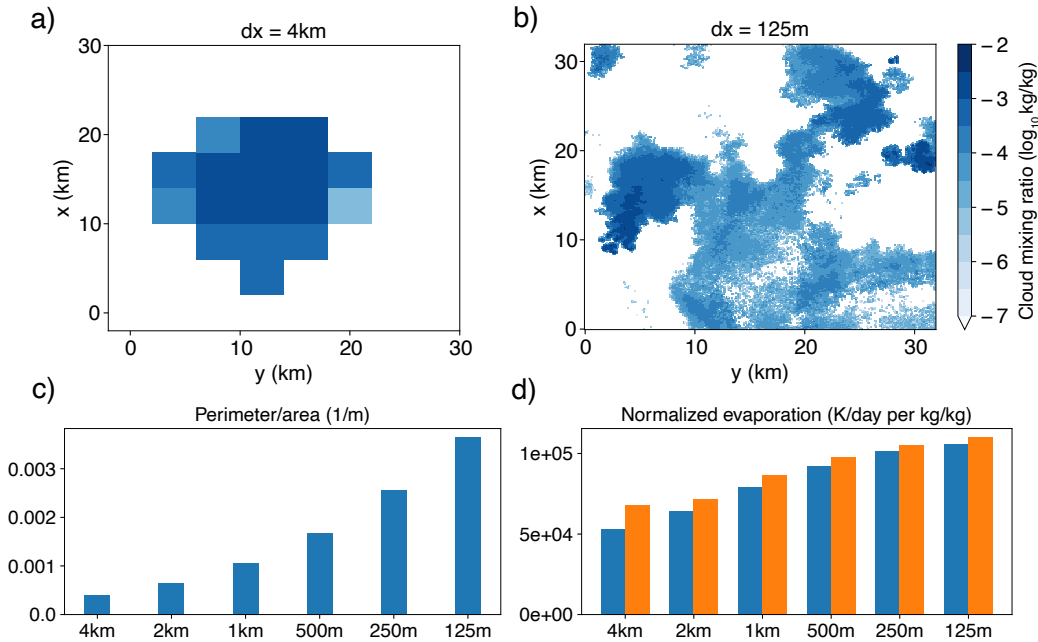


Figure 4. The upper row shows the cloud mixing ratio snapshots at $z=10\text{km}$ in a $32\text{km}\times 32\text{km}$ subdomain in the SAM1MOM simulations with grid size of 4km (a) and 125m (b). Panel c shows the perimeter area ratio in the SAM1MOM simulations with different grid size. Panel d shows the normalized evaporation in Fig. 3f at $z=10\text{km}$. Blue bars are direct model diagnostic values, and orange bars are estimated by Equation 4.

338 We further dissect the radiation-driven subsidence into radiation and stability components.
 339 The radiative cooling shows slight non-monotonic changes (Fig. 5d), while the
 340 upper troposphere is less stable with finer resolution (Fig. 5e and 5f). The change in sta-
 341 bility can be associated with the shift in the entrainment rate (Fig. 6), which tends to
 342 increase with finer resolution. We illustrate this entrainment change with a model of a
 343 spectrum of entraining plumes, following the approach of Kuang and Bretherton (2006).
 344 In this spectrum plume calculations, we use environmental profiles from each simulation
 345 to infer the entrainment rate for updrafts. In Fig. 6a and 6c, we show the convective
 346 mass flux distribution in the space of frozen moist static energy (FMSE) and height.
 347 FMSE is defined as $c_p T + gz + L_v q - L_f q_i$. The individual lines represent the FMSE
 348 profiles of entraining plumes rising from the cloud base with different entrainment rates.
 349 The convective updrafts in the 125m -resolution simulation (Fig. 6c) shift towards FMSE
 350 profiles with higher entrainment rate compared to the updrafts in the 4km -resolution sim-
 351 ulation (Fig. 6a). Once we have computed the FMSE profiles with varying entrainment
 352 rates, we can measure the amount of mass flux allocated to each entrainment rate bin.
 353 Subsequently, we can represent the updraft mass flux in the space of height and entrain-
 354 ment rate. As shown in Fig. 6b and 6d, it is apparent that the mass flux distribution
 355 shifts towards higher entrainment rates with finer resolution. We have done similar anal-
 356 ysis for the SAM1MOM simulations (not shown) and found consistent results that finer
 357 resolution tends to have higher entrainment rates. However, it is important to note that
 358 the sensitivity of entrainment rate on grid size could be model dependent. In the SAM
 359 model we use, the entrainment mixing seems to be contributed mainly by numerical dif-
 360 fusion, while sub-grid diffusion is very weak in free troposphere. Whether the resolution
 361 dependence of the entrainment rate would hold with other models using different advec-
 362 tion scheme and sub-grid diffusion scheme needs to be further tested.

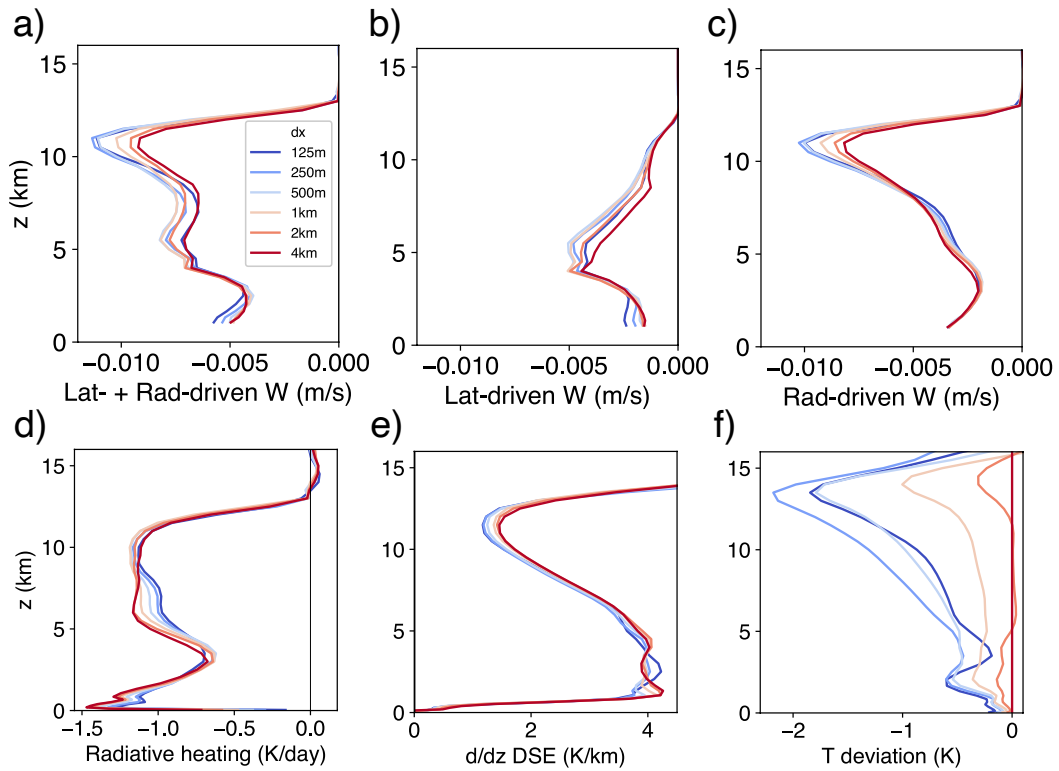


Figure 5. Energy budget for environmental subsidence for the Morrison simulations. The first row shows the subsidence contributed by latent heat (panel b), by radiative cooling (panel c), and by both (a). Panel d shows the radiative heating rate averaged in environments. Panel e shows the vertical gradient of dry static energy averaged in environments. Panel f shows the absolute temperature profiles as deviation to the 4km Morrison simulation.

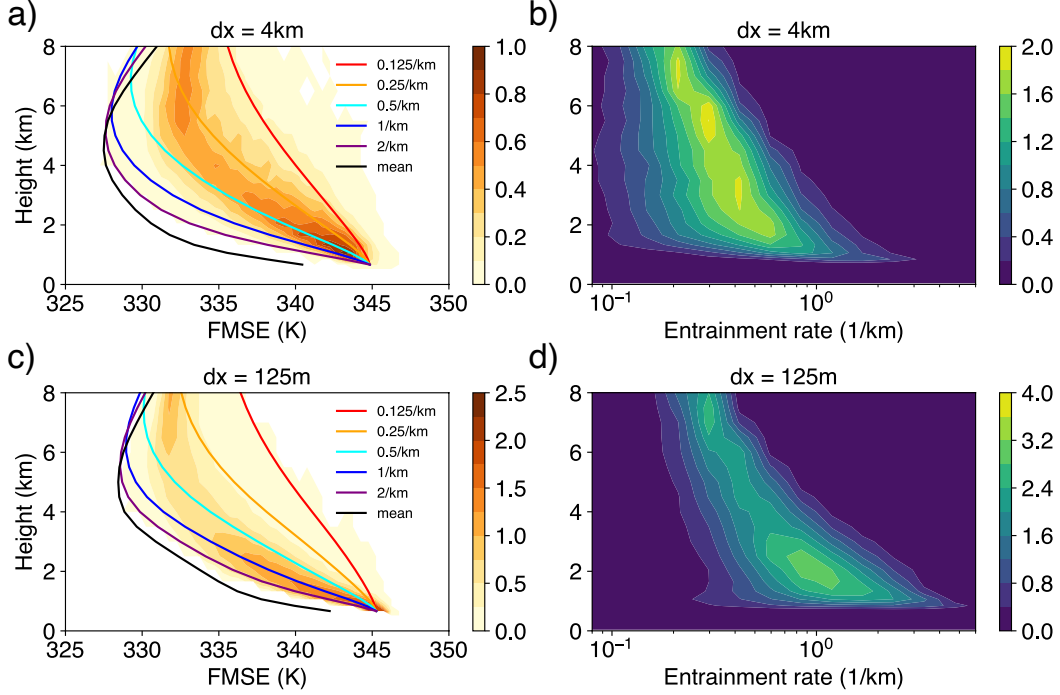


Figure 6. The distribution of convective updraft mass flux in FMSE-height space (left column) and in entrainment-height space (right column) for grid size of 4km (upper row) and of 125m (lower row). In the left column, we show the mass flux distribution (with a unit of a unit of $kg\ m^{-2}\ s^{-1}\ bin^{-1}$) binned by their FMSE (in unit of K). There are 50 bins with 0.5K interval between 325K to 350K. The individual lines represent the FMSE profiles of entraining plumes rising from cloud base with different entrainment rates, except the black line which represents domain-mean FMSE profiles. In the right column, we show the mass flux distribution (with a unit of a unit of $kg\ m^{-2}\ s^{-1}\ bin^{-1}$) binned by their effective entrainment rate. The bin boundaries have entrainment rates of $2^{(i/2)-4}$, for $i = 0, 1, 2, \dots, 16$, with a unit of km^{-1} . We calculated the instantaneous FMSE profiles with these different entrainment rates and sorted the convective updraft mass flux by these different entraining moist-adiabat FMSE values.

Fig. 7 explores the reasons behind the distinctive environmental energy balance regime observed in the Morrison simulations compared to the SAM1MOM simulations. In the Morrison simulations, the cooling effect from evaporation in the upper troposphere is notably weaker than that from radiation. Two factors could account for this subdued evaporation: diminished updrafts and a slower evaporation rate. As previously noted, the Morrison scheme tends to generate more anvil clouds, probably due to the significantly slower ice sedimentation removal rate and prolonged lifetime (refer to Fig. 2). The enhanced cloud radiative heating in the Morrison simulations could stabilize the upper troposphere, thereby reducing the intensity of updrafts. When we disable cloud radiative effects in the Morrison simulations (represented by solid lines in Fig. 7), we observe an increase in upper troposphere convective updrafts and stronger latent-driven subsidence, compared to the default Morrison simulations (dotted lines in Fig. 7). Additionally, the Morrison scheme does not employ saturation adjustment for cloud ice, potentially slowing evaporation compared to the SAM1MOM scheme. When we deactivate the cloud radiative effect and accelerate the cloud ice sublimation rate 100 times to mimic the saturation adjustment (dashed lines in Fig. 7), the result is faster evaporation and intensified updrafts. Consequently, latent-driven subsidence now contributes comparably to radiation-driven subsidence in modifying total subsidence near anvil level as resolution becomes finer (see Fig. 7b to d).

3.3 Insights from an analytical plume model

In the previous section, we presented that stronger horizontal mixing in finer-resolution simulations can enhance cloud evaporation and weaken the stability through a stronger entrainment rate. Both factors could potentially contribute to an enhanced convective updraft mass flux through the energy balance of environmental subsidence. However, a budget analysis does not necessarily reveal causality. Thus, in this section, we employ an analytical plume model to qualitatively explore the separate causal effects of changes in cloud evaporation and entrainment. This dissection of entrainment and evaporation effects offers us the opportunity to refine our understanding of the mechanism that bridges horizontal mixing with convective updraft mass flux.

The analytical plume model we use here is adapted from the zero-buoyancy plume model in Singh and Neogi (2022), with further references to Romps (2014), Singh et al. (2019), and Romps (2021). Here we provide a brief description of the model setup with the full description in Appendix B. The model presented in Singh and Neogi (2022) includes a thermodynamic component and a dynamic component. The thermodynamic component solves the equilibrium state of a moist atmosphere, and the dynamic component couples the thermodynamic component to large-scale circulation. In this study, we utilize only the thermodynamic model to examine radiative-convective equilibrium with no large-scale vertical velocity. It's crucial to distinguish between the analytical plume model used in this section and the spectrum plume model used for calculating the entrainment rate in the previous section. The latter utilizes the environmental profile from each simulation to determine a spectrum of entrainment rates for updrafts. Conversely, the analytical plume model in this section solves for the environmental profiles based on given surface boundary conditions and specified mixing strength and evaporation rate.

The thermodynamic model assumes that the steady state of the atmosphere can be represented by updrafts in a single updraft plume and downdrafts in environment. The updraft and environment can exchange mass, water, and heat via entrainment and detrainment. The model assumes that the steady state of the atmosphere is neutrally buoyant with respect to the entraining plume (Singh & O'Gorman, 2013). The model further presumes that the radiative cooling rate is a function of temperature, i.e., $-1K day^{-1}$ when the temperature is above 250K, and gradually decays to 0 at 200K. By solving conservation equations of mass, water vapor, and moist static energy, this model can solve the vertical atmosphere profiles given surface boundary conditions.

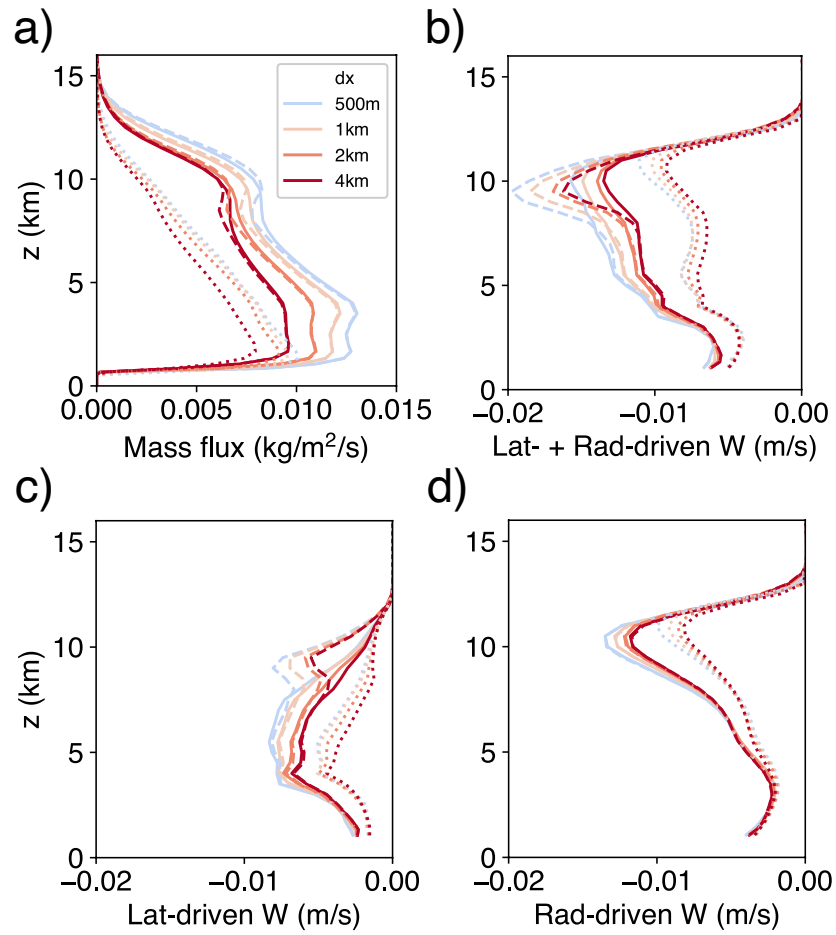


Figure 7. Convective updraft mass flux and energy budget for environmental subsidence in modified Morrison simulations. Solid lines represent simulations where cloud radiative effects are deactivated. Dashed lines indicate simulations with both cloud radiative effects deactivated and expedited cloud ice sublimation. Dotted lines represent default Morrison simulations. Panel a displays the convective updraft mass flux. Panels b to d present the subsidence contributions from latent heat (panel c), radiative cooling (panel d), and a combination of both (panel b).

One caveat of the solutions provided in Singh and Neogi (2022) and Romps (2021) is the assumption of equal fractional entrainment rate and detrainment rate, which in principle should suggest no vertical change in the convective updraft mass flux through the mass conservation equation:

$$\frac{\partial M_c}{\partial z} = M_c(\epsilon - \delta) \quad (5)$$

where M_c is updraft mass flux, ϵ is fractional entrainment rate, and δ is fractional detrainment rate. However, their solution of mass flux profile, e.g., Fig. 7 in Singh and Neogi (2022), does not follow this assumption, especially in the upper troposphere where mass flux rapidly decreases. In this study, we developed a self-consistent method of solving the equations by allowing the difference between fractional detrainment rate and fractional entrainment rate to vary vertically and not imposing any vertically structure on mass flux profile. The shape of the mass flux profile is partially constrained by energetics, as the mass flux needs to diminish where radiative cooling starts to rapidly decrease in the upper troposphere. Therefore, the entrainment rate and detrainment rate cannot be completely independent. Yet, one must still specify the strength of turbulent mixing in the model. This could be represented by either the entrainment rate, detrainment rate, or some other variable, such as the mixing rate in Bretherton et al. (2004). Here we choose to specify the entrainment rate to impose the strength of turbulent mixing. Once we specify the fractional entrainment rate profile (ϵ) and an evaporation parameter (μ), we can determine the vertical atmosphere profiles given boundary conditions (temperature, pressure, and relative humidity at cloud base).

In this model, cloud evaporation is parameterized as:

$$s_{evap} = \mu d(q^* - q) \quad (6)$$

where d is mass detrainment, q^* and q is the specific humidity in saturated updraft and in environment. A larger evaporation parameter μ tends to produce more cloud evaporation in the environment. This equation has two underlying assumptions. First, this equation assumes that the detrained flux of condensate is proportional to detrained flux of water vapor, represented by dq^* . A component of μ quantifies this relationship, representing the amount of condensate present in the detrained air. Second, it assumes that the fraction of detrained condensate that evaporates - as opposed to precipitating to the ground - is proportional to $1 - q/q^*$, which equates to $1 - RH$. A component of μ quantifies this relationship, reflecting the relative rates of evaporation versus conversion to rain. It is likely that the ratio of condensate evaporation versus conversion to rain is less sensitive to RH when RH is far less than 1. We also explored a different parameterization defined by $s_{evap} = \mu dq^*(1 - RH)^{0.5}$, which yielded results that are qualitatively similar (not shown). The full details of the model equations, derivation of the solution, and some sensitivity tests are documented in Appendix B.

With this model, we now test the sensitivity of the steady-state atmosphere profiles to entrainment rate and evaporation rate. First, we test the sensitivity to the fractional entrainment rate ϵ for two different values of the evaporation parameter μ (Fig. 8, upper row for $\mu = 1$ and lower row for $\mu = 0.1$). In both cases, with an increase in entrainment rate, we observe an increase in detrainment rate, mass flux, relative humidity, and the amount of latent cooling in the environment. The temperature in the upper troposphere is colder with a higher entrainment rate, and the stability (ds/dz) is lower. Fig. 8 suggests that increasing entrainment rate can lead to a relatively uniform increase of mass flux from cloud base to anvil level, although the budget for environmental subsidence can look like different regimes.

Considering the dry static energy budget $M_c = (Q_{rad} + Q_{lat})/(\frac{\partial s}{\partial z})$, increasing entrainment rate leads to both increasing cloud evaporation and more unstable upper troposphere. Both these two factors can contribute to an increasing mass flux. When cloud evaporation is efficient (Fig. 8 with $\mu = 1$), the change of latent cooling can dominate the change of mass flux. However, when cloud evaporation is weak (Fig. 8 with $\mu =$

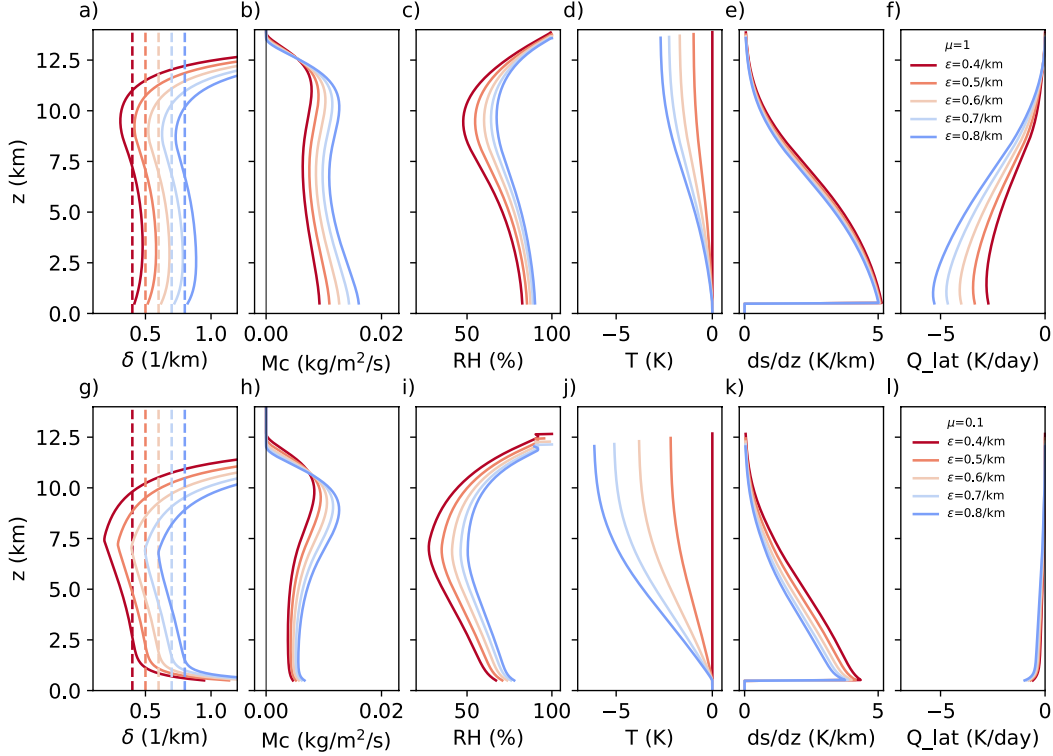


Figure 8. Atmosphere profiles in the zero-buoyancy plume model with varying entrainment rates (warmer color represents lower entrainment rate). The upper row has a cloud evaporation parameter $\mu=1$. The variables shown are detrainment rate (a), updraft mass flux (b), relative humidity (c), temperature (d), vertical gradient of dry static energy (e), and latent heating rate due to cloud evaporation in the environment (f). Dashed lines in panel a are the profiles of prescribed entrainment rate. The temperature in panel d is shown as deviation to one of the simulations, which is denoted by the red line with zero deviation. The lower row is similar to the upper row but with cloud evaporation parameter $\mu=0.1$.

467 0.1), the absolute latent cooling and the change of latent cooling is small compared to
 468 the prescribed radiative cooling. The change of stability to increasing entrainment rate
 469 is larger with small μ and can dominate the change of mass flux. Environmental rela-
 470 tive humidity is important in determining the sensitivity of stability to changing entrain-
 471 ment rate. The relative humidity is smaller with $\mu=0.1$ than $\mu=1$ (Fig. 8c and i). Since
 472 entrainment affects stability through the environmental saturation deficit, a small μ tends
 473 to make stability more sensitive to the change of entrainment (Fig. 8e and k).

474 The energy balance regime with small evaporation parameter resembles that in the
 475 Morrison simulations in the previous section. The Morrison scheme likely has a smaller
 476 evaporation parameter for cloud ice evaporation than the SAM1MOM scheme, due to
 477 the avoidance of saturation adjustment in Morrison scheme, potentially contributing to
 478 the weak absolute latent cooling rate. However, the stability change is not that large be-
 479 tween Morrison and SAM1MOM scheme, comparing to the difference between the ana-
 480 lytical plume results with $\mu=0.1$ and $\mu=1$. The Morrison simulations also have slightly
 481 higher relative humidity in the upper troposphere compared to the SAM1MOM simu-
 482 lations. The main difference between the Morrison and the SAM1MOM simulations is
 483 the diminished environmental latent cooling instead of the stability change.

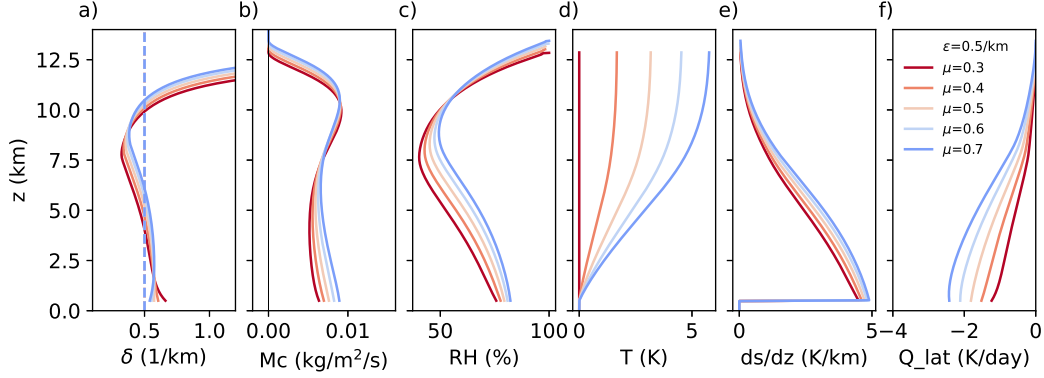


Figure 9. Similar to Fig. 8 but with fixed entrainment rate of 0.5 km^{-1} and varying cloud evaporation parameter (warmer color represents less efficient cloud evaporation).

484 In Fig. 9, we maintain a constant fractional entrainment rate as 0.5 km^{-1} and test
 485 the sensitivity of atmosphere profiles to the evaporation parameter μ . As the evapora-
 486 tion strength increases, we can see that the free troposphere is warmer, deeper, and more
 487 moist (Fig. 9b,9c,9d). The increased relative humidity is a direct result of the enhanced
 488 efficiency of cloud evaporation. This is consistent with JZ22 which shows that the evap-
 489 oration efficiency plays an important role for the relative humidity, especially in the up-
 490 per troposphere. Consequently, with a more moist atmosphere, the dilution of the up-
 491 draft plume due to entrainment is mitigated, resulting in a warmer and elevated tropo-
 492 sphere. In lower troposphere, we see a clear increase of mass flux with increasing cloud
 493 evaporation. However, in the upper troposphere, the mass flux adjustment is more akin
 494 to a upward shift with weak change in magnitude. The peak mass flux near the anvil
 495 level remains largely unchanged, suggesting a minor change in the convergence of mass
 496 flux at higher altitudes. From the perspective of the energy budget, an increase in the
 497 evaporation rate could induce greater latent cooling. However, this is offset by an increase
 498 in stability in the upper troposphere, effectively suppressing the change in mass flux (Fig.
 499 9e and 9f).

500 From Fig. 8 and Fig. 9, we can see that the resolution dependence of updraft mass
 501 flux may not necessarily be driven by evaporation efficiency alone. However, updraft mass
 502 flux can simply be interpreted as a response to the change of entrainment rate or the strength
 503 of horizontal mixing. In addition to the energy budget, a different way to understand
 504 the mass flux response to entrainment rate change in this analytical model is through
 505 the Betts’s rule described in Jeevanjee (2022). Considering the water vapor budget for
 506 the atmosphere above a certain level z . The mass flux at z satisfies:

$$507 \quad M_c q^* (1 - RH) = \int_z^{top} -c_p \rho Q_{rad} dz / L_v \quad (7)$$

508 where q^* is the saturation vapor mixing ratio, c_p is the isobaric specific heat, ρ is air den-
 509 sity, L_v is the latent heat of vaporization. The left hand side (LHS) represents the net
 510 water vapor transported upward across level z by saturated updraft and unsaturated sub-
 511 sidence. In steady state, this transport of vapor must be balanced by the net conden-
 512 sation, which is required to balance the total radiative cooling above level z (the right
 513 hand side, RHS). Since in the model the prescribed the radiative cooling is constant at
 514 -1 K day^{-1} for troposphere where temperature is larger than 250K, the change in RHS
 515 is relatively small, especially for the lower and middle troposphere. When we increase
 516 the horizontal mixing (Fig. 8), the relative humidity increases, and more clouds get de-
 517 trained. The temperature through the whole troposphere also decreases, leading to a de-

518 creasing saturation vapor mixing ratio q^* . To satisfy the equation, the mass flux on the
 519 LHS has to increase to provide enough upward vapor transport.

520 4 Conclusions and Discussion

521 In this work, we investigated the mechanisms underlying the dependence of anvil
 522 cloud fraction on horizontal model resolution in small domain radiative-convective equi-
 523 librium (RCE) simulations. Our findings indicate that finer resolutions yield a larger anvil
 524 cloud fraction due to increased convective updrafts mass flux and enhanced mass detrain-
 525 ment at anvil levels, aligning with Jeevanjee and Zhou (2022) (hereafter JZ22). Further
 526 examination revealed contributing processes to the mass flux increase near the anvil level.
 527 We leveraged two distinct microphysics schemes—one a single-moment scheme, the other
 528 a double-moment Morrison scheme—to reveal that finer resolutions enhance cloud evap-
 529 oration efficiency and entrainment rate, both of which are the consequence of enhanced
 530 horizontal mixing and could contribute to changes in mass flux.

531 In addition, we used an analytical zero-buoyancy plume model (Romps, 2014; Singh
 532 et al., 2019; Romps, 2021; Singh & Neogi, 2022) to further examine the mechanisms link-
 533 ing horizontal mixing to the change of mass flux. We refined the analytical plume model
 534 to derive self-consistent solutions of steady-state atmosphere profiles. This analytical model
 535 can serve as a simple, nice framework to understand general behaviors of RCE. Here, this
 536 model was employed to independently test the effects of modifying fractional entrain-
 537 ment rate and evaporation rate on mass flux and other atmospheric variables. Our anal-
 538 ysis revealed that increasing the fractional entrainment rate bolsters mass flux at both
 539 cloud base and near anvil level, whereas solely augmenting the evaporation rate primar-
 540 ily intensifies the mass flux in the lower troposphere with minimal impact on mass flux
 541 in the upper troposphere. By increasing the fractional entrainment rate alone, we ob-
 542 served that the increase of updraft mass flux can be attributed to either stronger latent
 543 cooling due to cloud evaporation or weaker upper-troposphere stability. The relative im-
 544 portance of these two processes may depend on evaporation rate. When the specified evap-
 545 oration rate is lower, environmental relative humidity is lower, and the lapse rate is more
 546 sensitive to the change of entrainment rate.

547 The results from analytical solution confirms that changes in the horizontal mix-
 548 ing can drive the resolution dependency of mass flux and cloud fraction found in the nu-
 549 merical simulations. One insight from our study, in comparison to JZ22, is that in cer-
 550 tain numerical simulations and analytical scenarios, the change in upper-tropospheric
 551 mass flux is predominantly driven by changes in stability resulting from modifications
 552 in the entrainment rate. Conversely, JZ22 attributes the increase of upper-tropospheric
 553 mass flux with finer resolution solely to the change in precipitation efficiency.

554 We observed that atmospheric profiles like cloud fraction and relative humidity start
 555 to converge when the grid size approximates 100m. The convergence when the grid size
 556 is at the order 100m may be linked to the convergence of entrainment rate and the mix-
 557 ing strength. We do not have a clear theory for the dependence of entrainment rate on
 558 horizontal resolution yet. A potential explanation is that coarser resolution inadequately
 559 resolves turbulent flow and cloud entrainment, and changes in sub-grid diffusion are in-
 560 sufficient to offset the changes in resolved turbulence. Bryan et al. (2003) demonstrated
 561 that a Smagorinsky-like sub-grid scheme is ill-suited for a grid size on the order of 1km.
 562 An inertial subrange can only manifest when the grid size is on the order of 100m. There-
 563 fore, it is plausible that once the grid size is sufficiently refined, changes in sub-grid dif-
 564 fusion can effectively counterbalance changes in numerical diffusion, leading to a con-
 565 vergence in entrainment rate and mixing strength. An ideal sub-grid turbulence param-
 566 eterization should make the entrainment strength scale insensitive even with resolution
 567 at the order of 1km. This might be one reason why Bogenschutz et al. (2023) found less
 568 sensitivity of high cloud fraction compared to this study and to JZ22.

569 The mechanisms we proposed is based on the radiative-convective equilibrium con-
 570 dition. Consequently, the resolution dependence of atmospheric profiles we observed may
 571 not persist when large-scale forcing overwhelms local convective adjustment or when a
 572 simulation has not reached an equilibrium state. This likely accounts for why Khairoutdinov
 573 et al. (2009) did not find the resolution dependence of cloud fraction with finer grid size
 574 in their 24-hour simulations with observed large-scale thermodynamic forcing.

575 Our study has implications to global storm-resolving simulations. Based on the con-
 576 vergence behavior in our small-domain simulations, the properties of cloud and convec-
 577 tion in global storm-resolving simulations may start to converge when the horizontal res-
 578 olution reaches the order of 100m. The exact resolution sensitivity can be model depen-
 579 dence. Also, it is not clear whether the same resolution dependence we learned in small-
 580 domain simulation—increasing resolution leading to more convective updrafts and cloud
 581 fraction—can be directly applied to the tropics in global storm-resolving simulations. The
 582 influence of horizontal resolution on cloud fraction or mass flux profiles could vary or even
 583 reverse if changing grid size changes the degree of large-scale aggregation of deep con-
 584 vection (e.g., Becker et al., 2017). Future research could focus on investigating these po-
 585 tential differences to better understand the uncertainties and biases inherent in global
 586 storm-resolving simulations.

587 5 Open Research

588 The atmosphere model used to run the simulations is the System for Atmospheric
 589 Modeling (Khairoutdinov & Randall, 2003) and is available at [http://rossby.msrc.sunysb](http://rossby.msrc.sunysb.edu/~marat/SAM.html)
 590 [.edu/~marat/SAM.html](http://rossby.msrc.sunysb.edu/~marat/SAM.html) (version 6.10.6, Khairoutdinov, 2023). The figures in this manuscripts,
 591 created by Python version 3.9, can be reproduced using the codes and data stored at [https://](https://doi.org/10.5281/zenodo.8397768)
 592 doi.org/10.5281/zenodo.8397768 (Hu et al., 2023).

593 Appendix A Relationship between cloud evaporation and perimeter 594 area ratio

595 In the preceding sections, we highlighted the increased perimeter area ratio of cloud
 596 mass at higher resolutions, which potentially leads to a greater exposure of the cloud mass
 597 to an unsaturated environment, thereby amplifying cloud evaporation. In this section,
 598 we derive a quantitative relationship between the cloud evaporation rate and the prime-
 599 ter area ratio.

600 Consider a specific level with a unit thickness, where the cloud mass has a total
 601 area (A) and total perimeter (L). The clouds are advected in grid points through resolved
 602 horizontal wind with a representative speed of U_{adv} . Approximately half of the cloud bound-
 603 ary exhibits horizontal resolved wind pointing outwards from the cloud, while the other
 604 half features wind directed inward (Fig. A1). After a time step dt , the volume of clouds
 605 advected across the boundary amounts to $0.5LU_{adv}dt$ (represented by the yellow area
 606 in Fig. A1a). An equivalent volume of environmental air is advected into the original
 607 cloudy grids (illustrated by the orange area in Fig. A1a). Following advection, the SAM1MOM
 608 scheme performs saturation adjustment. The yellow cloud mass becomes fully mixed with
 609 the environmental air in the respective grids, subsequently evaporating. On average, since
 610 the cloud mixing ratio near cloud edges is relatively minimal, we assume complete evap-
 611 oration of the yellow cloud mass. The evaporation associated with this yellow cloud mass
 612 should be proportional to the product of the volume and the cloud mixing ratio at the
 613 edge $q_{c,edge}$. Similarly, in the grids containing orange environmental air, a portion of the
 614 cloud must evaporate to bring the unsaturated orange environmental air to saturation.
 615 The evaporation amount would be the product of the volume and the saturation deficit
 616 $q_{v,env}^*(1 - RH)$, where $q_{v,env}^*$ represents the environmental saturation specific humid-
 617 ity and RH denotes relative humidity. The total evaporation rate associated with sat-

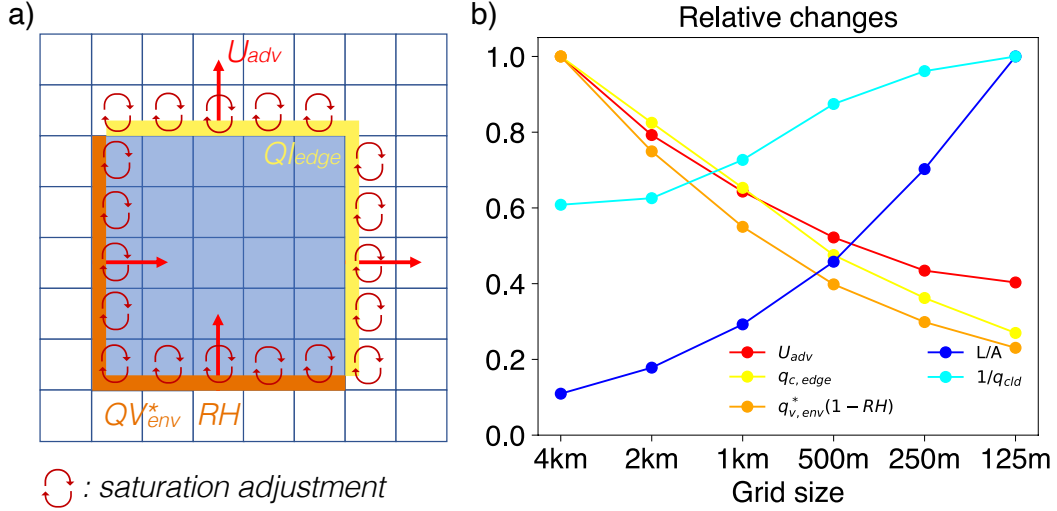


Figure A1. Panel a shows a schematic of cloud evaporation due to resolved horizontal advection and the following saturation adjustment in the SAM1MOM scheme. We set some cloud initially in the grids with blue shading and advect the cloud by horizontal wind with $U_x = U_y = U_{adv}$. $q_{c,edge}$ is the cloud mixing ratio near the cloud edge. $q_{v,env}^*$ represents the environmental saturation specific humidity, and RH denotes relative humidity in the environment near the cloud. After a small timestep dt , some cloud mass is advected into environment grids (yellow shading), and some environmental mass is advected into cloudy grids (orange shading). Circular arrows represent the saturation adjustment in each grid due to microphysics scheme. Panel b shows the relative value of different terms in Equation A4 in the SAM1MOM simulations with different resolution. Each term is standardized (divided by the maximum value across the simulations with different resolution) to have a value between 0 and 1.

618 uration adjustment can be expressed as:

$$619 \quad \text{Evaporation} = 0.5LU_{adv}\rho[q_{c,edge} + q_{v,env}^*(1 - RH)] \quad (\text{A1})$$

620 We assume all this evaporation can be counted as in the environment. We further as-
 621 sume the total evaporation in the environment is dominated by this numerical diffusion
 622 associated with resolved horizontal wind. This assumption likely works well for high clouds
 623 where vertical wind and sub-grid diffusion are weak, but may not work well for low clouds
 624 where vertical wind and sub-grid diffusion could be strong. Total air mass in the envi-
 625 ronment can be written as $\rho A_d f_{env}$, where A_d is domain area, f_{env} is the fraction of en-
 626 vironment. Therefore, the latent heating rate in the environment can be written as:

$$627 \quad Q_{lat,env} = 0.5LU_{adv}[q_{c,edge} + q_{v,env}^*(1 - RH)] \frac{L_v}{c_p A_d f_{env}} \quad (\text{A2})$$

628 Since more clouds tend to generate more evaporation, we normalize the latent heating
 629 by the total cloud mass to get a quantity that reflect evaporation efficiency. Total cloud
 630 mass is proportional to the domain-mean cloud mixing ratio q_m , which can be further
 631 expressed as $q_m = f_{cld} q_{cld}$. f_{cld} is cloud fraction, and q_{cld} is the cloud mixing ratio av-
 632 eraged in cloudy grids. The normalized latent heating rate can be expressed as:

$$633 \quad \frac{Q_{lat,env}}{q_m} = 0.5LU_{adv}[q_{c,edge} + q_{v,env}^*(1 - RH)] \frac{L_v}{c_p A_d f_{env} f_{cld} q_{cld}} \quad (\text{A3})$$

634 Note that total cloud area can be written as $A = f_{cld} A_d$, the above equation can be
 635 rewritten as:

$$636 \quad \frac{Q_{lat,env}}{q_m} = \frac{L}{A} U_{adv} \frac{q_{c,edge} + q_{v,env}^*(1 - RH)}{q_{cld}} \frac{L_v}{2c_p f_{env}} \quad (\text{A4})$$

637 We define cloud boundaries as grid interfaces that separate a grid with zero cloud
 638 mixing ratio from a grid with non-zero cloud mixing ratio. Subsequently, we evaluate
 639 the average values of U_{adv} , $q_{c,edge}$, $q_{v,env}^*$, and RH at grids immediately adjacent to the
 640 boundaries, either on the inside or the outside. In Fig. A1b, we demonstrate the vari-
 641 ation in different terms of Equation A4 as resolution becomes finer. With increased res-
 642 olution, the perimeter area ratio rises, while advection velocity, cloud mixing ratio, and
 643 environmental saturation deficit decrease. The decline in near-edge cloud mixing ratio
 644 and environmental saturation deficit could be attributed to the improved representation
 645 of the transition between cloudy grids and environmental grids at finer scales. The en-
 646 hanced transition at cloud boundaries in higher resolutions tends to reduce numerical
 647 diffusion and partially counterbalance the effect of the growing perimeter area ratio. The
 648 cause of the weakened advection wind and reduced in-cloud mixing ratio remains unclear
 649 and merits further investigation.

650 Overall, finer resolution enables better representation of turbulent cloud bound-
 651 aries, which can enhance the interaction between clouds and their environment. How-
 652 ever, finer resolution also leads to a reduction in numerical diffusion. The interplay be-
 653 tween these two effects may be crucial in determining whether cloud evaporation effi-
 654 ciency converges at a specific resolution. A comprehensive understanding of these fac-
 655 tors is essential for improving the accuracy and reliability of Earth system models.

656 **Appendix B Refined solutions of a zero-buoyancy plume model**

657 Here we document the details of how we solve the zero-buoyancy plume model to
 658 get self-consistent solutions about steady-state mass flux, detrainment rate, and other

659 atmosphere profiles. The equations we solve are:

$$660 \quad \frac{\partial M_c}{\partial z} = e - d \quad (\text{B1})$$

$$661 \quad M_c + M_e = 0 \quad (\text{B2})$$

$$662 \quad \frac{\partial(M_c q^*)}{\partial z} = e q - d q^* - s_{cond} \quad (\text{B3})$$

$$663 \quad \frac{\partial(M_e q)}{\partial z} = d q^* - e q + s_{evap} \quad (\text{B4})$$

$$664 \quad \frac{\partial(M_c h^*)}{\partial z} = e h - d h^* \quad (\text{B5})$$

$$665 \quad \frac{\partial(M_e h)}{\partial z} = d h^* - e h + Q_{rad} \quad (\text{B6})$$

$$666 \quad h^* - h = L_v (q^* - q) \quad (\text{B7})$$

$$667 \quad s_{evap} = \mu d (q^* - q) \quad (\text{B8})$$

$$668 \quad \frac{\partial p}{\partial z} = -\frac{\rho g}{R_d T} \quad (\text{B9})$$

670 Equation B1 and B2 are mass conservation equations. M_c is the mass flux of con-
 671 vective updrafts, and M_e is mass flux in the environment. We assume there is no large-
 672 scale advection, so the net mass flux in updrafts and in environment is 0. e is mass en-
 673 trainment, and d is mass detrainment. Fractional entrainment rate ϵ and fractional de-
 674 trainment rate δ are defined as:

$$675 \quad \epsilon = e/M_c \quad (\text{B10})$$

$$676 \quad \delta = d/M_c \quad (\text{B11})$$

678 Equation B3 and B4 describes the water vapor conservation in updraft plume and
 679 in environment separately. q is the water vapor mixing ratio in the environment. q^* is
 680 the saturation vapor mixing ratio in the updraft plume, which is simply a function of
 681 temperature and pressure:

$$682 \quad q^* = 0.622 p_v^*/p = 0.622 \frac{p_0}{p} e^{-\frac{L_v}{R_v T}} \quad (\text{B12})$$

684 where $p_v^* = p_0 \exp(-L_v/(R_v T))$ is the saturation vapor pressure, $L_v=2.51e6 \text{ J kg}^{-1}$
 685 is the latent heat of condensation, $R_v= 461 \text{ J kg}^{-1} \text{ K}^{-1}$ is gas constant for water vapor,
 686 $p_0=2.69e11 \text{ Pa}$ is a constant.

687 Equation B5 and B6 describes the conservation of moist static energy in updraft
 688 plume and in environment. $h = c_p T + gz + L_v q$ is the moist static energy in the en-
 689 vironment, and $h^* = c_p T + gz + L_v q^*$ is the saturation moist static energy in the up-
 690 draft plume. We specify radiative heating rate to be simply a function of temperature,

$$691 \quad Q_{rad}/(c_p \rho) = \begin{cases} Q_0, & \text{if } T > 250K \\ Q_0(0.5 + 0.5 \cos(\pi(250 - T)/(250 - 200))), & \text{if } 250K > T > 200K \\ 0, & \text{if } T < 200K \end{cases} \quad (\text{B13})$$

693 where $Q_0 = -1Kday^{-1}$. Radiative heating rate is constantly $-1Kday^{-1}$ in lower and
 694 middle troposphere and gradually decays to 0 from $T=250K$ to $T=200K$. $\rho = p/R_d T$
 695 is the air density.

696 Equation B7 implies the zero-buoyancy assumption that the temperature in up-
 697 drafts is the same as the temperature in the environment at the same height. Equation
 698 B8 is the parameterization of cloud evaporation in the environment, following the def-
 699 inition in the Singh and Neogi (2022). μ is a unitless parameter which controls the speed
 700 of cloud evaporation. We assume cloud evaporation happens at the level where cloud is

701 condensed, and we assume there is no evaporation of precipitation. Equation B9 is the
702 hydrostatic balance, and $R_d = 287 J kg^{-1} K^{-1}$ is the gas constant for dry air.

703 For Equation B1 to B9, there are 9 equations but 11 unknown variables: M_c , M_e ,
704 ϵ , δ , q^* , q , h , s_{cond} , s_{evap} , μ , and p . We have excluded h^* and Q_{rad} from unknown vari-
705 ables since they can be expressed using h^* and p through Equation B12 and B13. We
706 take ϵ and μ to be the free parameters that we can specify, and the rest of the equations
707 is just enough to get self-consistent solution. If one further specifies δ , then there will
708 be more equations than unknown variables, in which case there cannot be self-consistent
709 solution. Next, we will describe how we solve these equations as an ODE problem and
710 express the equations as $\frac{\partial}{\partial z}(M_c, p, q, T) = F(M_c, p, q, T)$.

711 Replacing Equation B1 into Equation B3 to B7, we can get:

$$712 \quad M_c \frac{\partial q^*}{\partial z} = -\epsilon(1 - RH)M_c q^* - s_{cond} \quad (B14)$$

$$713 \quad M_e \frac{\partial q}{\partial z} = \delta(1 + \mu)(1 - RH)M_c q^* \quad (B15)$$

$$714 \quad M_c \frac{\partial h^*}{\partial z} = -\epsilon L_v(1 - RH)M_c q^* \quad (B16)$$

$$715 \quad M_e \frac{\partial h}{\partial z} = \delta L_v(1 - RH)M_c q^* + Q_{rad} \quad (B17)$$

717 $RH = q/q^*$ is the relative humidity in the environment.

718 Equation B1 can be rewritten as:

$$719 \quad \frac{\partial M_c}{\partial z} = M_c(\epsilon - \delta) \quad (B18)$$

721 Using Equation B2 and B15, we get:

$$722 \quad \frac{\partial q}{\partial z} = -\delta(1 + \mu)(1 - RH)q^* \quad (B19)$$

724 Equation B16 can be used to express the temperature lapse rate $\Gamma = -\frac{\partial T}{\partial z}$. From
725 the definition of h^* , we have:

$$726 \quad \frac{\partial h^*}{\partial z} = -c_p \Gamma + g + L_v \frac{\partial q^*}{\partial z} \quad (B20)$$

728 Using Equation B9 and B12 and defining $\gamma = -(1/q^*)\frac{\partial q^*}{\partial z}$, we can get:

$$729 \quad \gamma = \frac{L_v \Gamma}{R_v T^2} - \frac{g}{R_d T} \quad (B21)$$

731 Replacing Equation B20 and B21 into Equation B16, we can get:

$$732 \quad \frac{\partial T}{\partial z} = \frac{1}{c_p + q^* L_v^2 / (R_v T^2)} [-g(1 + \frac{L_v q^*}{R_d T}) - \epsilon L_v(1 - RH)q^*] \quad (B22)$$

734 When we sum Equation B3 and B4, sum Equation B5 and B6, and use Equation
735 B2 and B7, we can get the energy balance equation:

$$736 \quad Q_{rad} = L_v(s_{cond} - s_{evap}) \quad (B23)$$

738 Replacing Equation B8 and B14 into Equation B23, we can get the expression of
739 M_c or δ :

$$740 \quad M_c = -\frac{Q_{rad}/(L_v q^*)}{\gamma - (\epsilon + \mu\delta)(1 - RH)} \quad (B24)$$

$$741 \quad \delta = -\frac{\epsilon}{\mu} + \frac{\gamma}{\mu(1 - RH)} + \frac{Q_{rad}}{\mu(1 - RH)q^* L_v M_c} \quad (B25)$$

743 Now with Equation B9, B18, B19, B22, and B25, we have the closed form expres-
 744 sion for our ODE problem:

$$745 \frac{\partial}{\partial z}(M_c, p, q, T) = F(M_c, p, q, T) \quad (B26)$$

747 where the right hand side only depends on M_c , p , q , and T . Given boundary conditions
 748 at cloud base (we use $z=500\text{m}$), Equation B26 can integrate upwards and get the full
 749 atmosphere profiles.

750 For boundary conditions, we specify a surface temperature of 303K and surface pres-
 751 sure of 10^5 Pa. We assume dry adiabatic lapse rate of $g/c_p = 9.8\text{Kkm}^{-1}$ below cloud
 752 base, and we can use Equation B9 to integrate pressure p from the surface to cloud base.
 753 For environmental water vapor mixing ratio q at cloud base, we do not have a solid con-
 754 strain. If one assumes $\frac{\partial q}{\partial z} \approx RH \frac{\partial q^*}{\partial z}$ (the vertical gradient of RH is much smaller than
 755 the vertical gradient of q^*), Equation B15 can reduce to:

$$756 RH = \frac{\delta(1 + \mu)}{\delta(1 + \mu) + \gamma} \quad (B27)$$

758 We determine our cloud base q using Equation B27, and the value of δ in Equation B27
 759 is taken from the ϵ . In this way, we implicitly assumes that increasing ϵ or μ can have
 760 a moistening effect at the cloud base, which intuitively makes sense. We will show later
 761 the sensitivity of solution to the value of cloud base q .

762 For M_c , we do not have a direct cloud base constrain. However, we assume our so-
 763 lution is in radiative-convective equilibrium (RCE), which says radiative cooling must
 764 be balanced by latent heat release at all the levels. The RCE condition requires that M_c
 765 reaches 0 exactly at the level where the radiative cooling rate becomes 0, i.e., at $T=200\text{K}$
 766 (Equation B13). If cloud base M_c is too large, M_c will still be positive where $T=200\text{K}$.
 767 If cloud base M_c is too small, M_c will go to 0 before radiative cooling decays to 0. We
 768 can have a random initial guess of cloud base M_c and change our guess based on this RCE
 769 condition. Once we find lower and upper bounds of the cloud base M_c , we use binary
 770 search to iteratively guess between the bounds and narrow the bounds until we find the
 771 M_c that satisfies the RCE condition.

772 In Fig. B1 we test the sensitivity of the atmospheric profiles to the cloud base wa-
 773 ter vapor mixing ratio (or equivalently RH). We change the cloud base RH from 70%
 774 to 90%. Except temperature profile, the influence of cloud base RH on other variables
 775 is primarily within the lower 5km and does not have a big impact to the upper tropo-
 776 sphere. The temperature becomes warmer through the whole troposphere with moister
 777 cloud base environment. For cloud base mass flux, it strongly depends on the RH based
 778 on Equation 5 in the main text. The way we determine the cloud base RH using Equa-
 779 tion B27 will implicitly lead to the sensitivity that cloud base mass flux increases when
 780 ϵ or μ increase. Since our main focus in this paper is the upper troposphere mass flux,
 781 the uncertainty in how we determine the cloud base RH will likely not change our re-
 782 sults. We also tested fixing the relative humidity at the cloud base. The sensitivities re-
 783 garding to mixing strength and evaporation rate remain qualitatively the same. In fu-
 784 ture research, it would be beneficial to integrate considerations of energy and water con-
 785 servation in the subcloud layer, along with surface flux parameterization, to automat-
 786 ically determine the cloud base relative humidity.

787 In Fig. B2 we test the sensitivity to different sea surface temperature. We can see
 788 that the whole troposphere becomes higher with the profiles of most quantities shifting
 789 upwards. The peak value of mass flux near the anvil level decreases with warmer sur-
 790 face temperature, which will indicate a weaker mass detrainment and likely a decrease
 791 of anvil cloud fraction (if lifetime is assumed to be unchanged with surface warming).
 792 The decrease of upper troposphere mass flux is consistent with the stability iris effect
 793 proposed in (Bony et al., 2016).

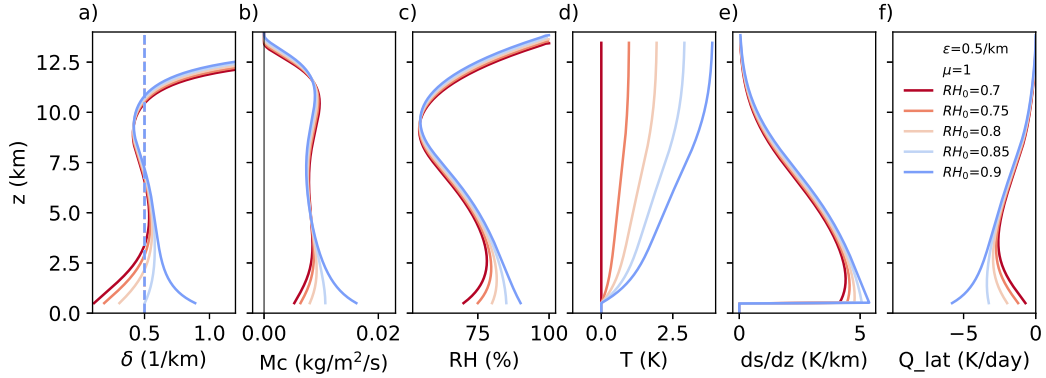


Figure B1. Atmosphere profiles in the zero-buoyancy plume model with varying cloud-base relative humidity (blue color represents more moist environment), entrainment rate $\epsilon = 0.5 \text{ km}^{-1}$, and cloud evaporation parameter $\mu = 1$. The variables shown are detrainment rate (a), updraft mass flux (b), relative humidity (c), temperature (d), vertical gradient of dry static energy (e), and latent heating rate due to cloud evaporation in the environment (f). Dashed lines in panel a are the profiles of prescribed entrainment rate. The temperature in panel d is shown as deviation to one of the simulations, which is denoted by the red line with zero deviation.

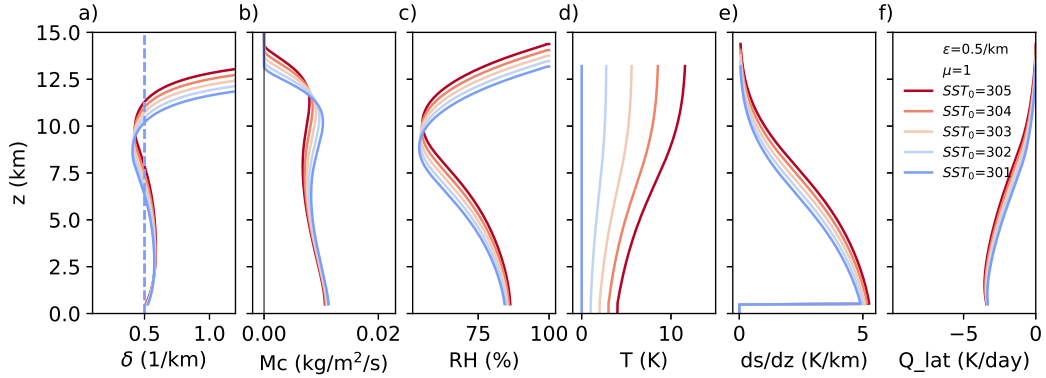


Figure B2. Similar to Fig. B1 but with sea surface temperature (blue color represents colder surface temperature), entrainment rate $\epsilon = 0.5 \text{ km}^{-1}$, and cloud evaporation parameter $\mu = 1$.

Acknowledgments

We thank Marat Khairoutdinov for making the SAM model available. ZH thanks Peter Blossey, Blaž Gasparini, Chris Bretherton, and Andrea Jenney for discussion/comments on this work. ZH and ZK acknowledge the funding from NSF Grant 1743753 and from the Office of Biological and Environmental Research of the U.S. DOE under grant DE-SC0022887 as part of the ASR Program. ZH acknowledges Grant DGE1745303 from NSF Graduate Research Fellowships Program.

References

- Becker, T., Stevens, B., & Hohenegger, C. (2017). Imprint of the convective parameterization and sea-surface temperature on large-scale convective self-aggregation. *Journal of Advances in Modeling Earth Systems*, *9*(2), 1488–1505.
- Beydoun, H., Caldwell, P. M., Hannah, W. M., & Donahue, A. S. (2021). Dissecting anvil cloud response to sea surface warming. *Geophysical Research Letters*, *48*(15), e2021GL094049.
- Bogenschutz, P. A., Eldred, C., & Caldwell, P. M. (2023). Horizontal resolution sensitivity of the simple convection-permitting e3sm atmosphere model in a doubly-periodic configuration. *Journal of Advances in Modeling Earth Systems*, *15*(7), e2022MS003466. Retrieved from <https://agupubs.onlinelibrary.wiley.com/doi/abs/10.1029/2022MS003466> (e2022MS003466 2022MS003466) doi: <https://doi.org/10.1029/2022MS003466>
- Bony, S., Stevens, B., Coppin, D., Becker, T., Reed, K. A., Voigt, A., & Medeiros, B. (2016). Thermodynamic control of anvil cloud amount. *Proceedings of the National Academy of Sciences*, *113*(32), 8927–8932.
- Bony, S., Stevens, B., Frierson, D. M., Jakob, C., Kageyama, M., Pincus, R., . . . others (2015). Clouds, circulation and climate sensitivity. *Nature Geoscience*, *8*(4), 261–268.
- Bretherton, C. S., McCaa, J. R., & Grenier, H. (2004). A new parameterization for shallow cumulus convection and its application to marine subtropical cloud-topped boundary layers. part i: Description and 1d results. *Monthly weather review*, *132*(4), 864–882.
- Bryan, G. H., Wyngaard, J. C., & Fritsch, J. M. (2003). Resolution requirements for the simulation of deep moist convection. *Monthly Weather Review*, *131*(10), 2394–2416.
- Hartmann, D. L., Gasparini, B., Berry, S. E., & Blossey, P. N. (2018). The life cycle and net radiative effect of tropical anvil clouds. *Journal of Advances in Modeling Earth Systems*, *10*(12), 3012–3029.
- Hohenegger, C., Kornblueh, L., Klocke, D., Becker, T., Cioni, G., Engels, J. F., . . . Stevens, B. (2020). Climate statistics in global simulations of the atmosphere, from 80 to 2.5 km grid spacing. *Journal of the Meteorological Society of Japan. Ser. II*, *98*(1), 73–91.
- Hu, Z., Jeevanjee, N., & Kuang, Z. (2023). From grid to cloud: Understanding the impact of grid size on simulated anvil clouds and atmospheric profiles [software]. doi: <https://doi.org/10.5281/zenodo.8397768>
- Hu, Z., Lamraoui, F., & Kuang, Z. (2021). Influence of upper-troposphere stratification and cloud–radiation interaction on convective overshoots in the tropical tropopause layer. *Journal of the Atmospheric Sciences*, *78*(8), 2493–2509.
- Iacono, M. J., Delamere, J. S., Mlawer, E. J., Shephard, M. W., Clough, S. A., & Collins, W. D. (2008). Radiative forcing by long-lived greenhouse gases: Calculations with the aer radiative transfer models. *Journal of Geophysical Research: Atmospheres*, *113*(D13).

- 847 Jeevanjee, N. (2017). Vertical velocity in the gray zone. *Journal of Advances in*
848 *Modeling Earth Systems*, 9(6), 2304–2316.
- 849 Jeevanjee, N. (2022). Three rules for the decrease of tropical convection with
850 global warming. *Journal of Advances in Modeling Earth Systems*, 14(11),
851 e2022MS003285.
- 852 Jeevanjee, N., & Zhou, L. (2022). On the resolution-dependence of anvil cloud frac-
853 tion and precipitation efficiency in radiative-convective equilibrium. *Journal of*
854 *Advances in Modeling Earth Systems*, 14(3), e2021MS002759.
- 855 Khairoutdinov, M. (2023). System for atmospheric modeling [software]. Retrieved
856 from <http://rossby.msrc.sunysb.edu/~marat/SAM/>
- 857 Khairoutdinov, M., Krueger, S. K., Moeng, C.-H., Bogenschutz, P. A., & Randall,
858 D. A. (2009). Large-eddy simulation of maritime deep tropical convection.
859 *Journal of Advances in Modeling Earth Systems*, 1(4).
- 860 Khairoutdinov, M., & Randall, D. A. (2003). Cloud resolving modeling of the arm
861 summer 1997 iop: Model formulation, results, uncertainties, and sensitivities.
862 *Journal of the Atmospheric Sciences*, 60(4), 607–625.
- 863 Kuang, Z., & Bretherton, C. S. (2006). A mass-flux scheme view of a high-resolution
864 simulation of a transition from shallow to deep cumulus convection. *Journal of*
865 *the Atmospheric Sciences*, 63(7), 1895–1909.
- 866 Miyamoto, Y., Kajikawa, Y., Yoshida, R., Yamaura, T., Yashiro, H., & Tomita, H.
867 (2013). Deep moist atmospheric convection in a subkilometer global simula-
868 tion. *Geophysical Research Letters*, 40(18), 4922–4926.
- 869 Morrison, H., Curry, J., & Khvorostyanov, V. (2005). A new double-moment micro-
870 physics parameterization for application in cloud and climate models. part i:
871 Description. *Journal of the atmospheric sciences*, 62(6), 1665–1677.
- 872 Powell, S. W., Houze, R. A., Kumar, A., & McFarlane, S. A. (2012). Comparison
873 of simulated and observed continental tropical anvil clouds and their radiative
874 heating profiles. *Journal of the Atmospheric Sciences*, 69(9), 2662–2681.
- 875 Romps, D. M. (2014). An analytical model for tropical relative humidity. *Journal of*
876 *Climate*, 27(19), 7432–7449.
- 877 Romps, D. M. (2021). Ascending columns, wtg, and convective aggregation. *Journal*
878 *of the Atmospheric Sciences*, 78(2), 497–508.
- 879 Satoh, M., Stevens, B., Judt, F., Khairoutdinov, M., Lin, S.-J., Putman, W. M., &
880 Düben, P. (2019). Global cloud-resolving models. *Current Climate Change*
881 *Reports*, 5, 172–184.
- 882 Seeley, J. T., Jeevanjee, N., Langhans, W., & Romps, D. M. (2019). Formation of
883 tropical anvil clouds by slow evaporation. *Geophysical Research Letters*, 46(1),
884 492–501.
- 885 Sherwood, S., Webb, M. J., Annan, J. D., Armour, K. C., Forster, P. M., Harg-
886 reaves, J. C., . . . others (2020). An assessment of earth’s climate sensitivity us-
887 ing multiple lines of evidence. *Reviews of Geophysics*, 58(4), e2019RG000678.
- 888 Siebesma, A., & Jonker, H. (2000). Anomalous scaling of cumulus cloud boundaries.
889 *Physical review letters*, 85(1), 214.
- 890 Singh, M. S., & Neogi, S. (2022). On the interaction between moist convection and
891 large-scale ascent in the tropics. *Journal of Climate*, 35(14), 4417–4435.
- 892 Singh, M. S., & O’Gorman, P. A. (2013). Influence of entrainment on the ther-
893 mal stratification in simulations of radiative-convective equilibrium. *Geophysi-
894 cal Research Letters*, 40(16), 4398–4403.
- 895 Singh, M. S., Warren, R. A., & Jakob, C. (2019). A steady-state model for the rela-
896 tionship between humidity, instability, and precipitation in the tropics. *Journal*
897 *of Advances in Modeling Earth Systems*, 11(12), 3973–3994.
- 898 Stevens, B., Satoh, M., Auger, L., Biercamp, J., Bretherton, C. S., Chen, X., . . .
899 others (2019). Dyamond: the dynamics of the atmospheric general circula-
900 tion modeled on non-hydrostatic domains. *Progress in Earth and Planetary*
901 *Science*, 6(1), 1–17.

- 902 Wing, A. A., Stauffer, C. L., Becker, T., Reed, K. A., Ahn, M.-S., Arnold, N. P.,
903 ... others (2020). Clouds and convective self-aggregation in a multimodel
904 ensemble of radiative-convective equilibrium simulations. *Journal of Advances*
905 *in Modeling Earth Systems*, 12(9), e2020MS002138.
- 906 Zelinka, M. D., Myers, T. A., McCoy, D. T., Po-Chedley, S., Caldwell, P. M., Ceppi,
907 P., ... Taylor, K. E. (2020). Causes of higher climate sensitivity in cmip6
908 models. *Geophysical Research Letters*, 47(1), e2019GL085782.